Research Square

Preprints are preliminary reports that have not undergone peer review.
They should not be considered conclusive, used to inform clinical practice,
or referenced by the media as validated information.

Precipitation governs structural uncertainty and physical attribution of drought trends

Xiao Zhang
https://orcid.org/0009-0002-9704-5581
Jiameng Xu
Zhaoyu Dong
Yuanyuan Luo
Yuanchao Fan
yuanchao.fan@sz.tsinghua.edu.cn

Tsinghua University https://orcid.org/0000-0002-3462-1820

Article

Keywords:

Posted Date: July 28th, 2026

DOI: https://doi.org/10.21203/rs.3.rs-10359563/v1

License: This work is licensed under a Creative Commons Attribution 4.0 International License.
Read Full License

Additional Declarations: There is **NO** Competing Interest.

Abstract

Global drought assessments frequently attribute drying trends to warming-induced evaporative demand represented by potential evapotranspiration (PET), yet the dominant physical mechanism and structural data uncertainty in drought trends remain poorly understood. Using a 240-member Standardized Precipitation Evapotranspiration Index (SPEI) super-ensemble over quasi-global land (50°S–50°N), we find substantial structural uncertainty of estimated drought trends, represented by a large inter-member standard deviation (± 0.0052 yr^{-1}) of quasi-global SPEI trend relative to the ensemble mean (– 0.0029 yr^{-1}). Our uncertainty decomposition analysis shows that precipitation-product discrepancies account for 71.5% of global-mean and 78.1% of grid-level SPEI trend variance during 1981–2024, far exceeding PET-related uncertainty. Three independent physical attribution frameworks consistently show that precipitation changes explain 66.0–74.6% of historical SPEI trends, with PET as a secondary contributor. Ensemble subsets combining gauge- or satellite-derived precipitation with energy-based PET formulations yield non-significant quasi-global drying (11 members) or even wetting trends (73 members), reflecting the sensitivity of apparent trends to precipitation forcing choices. Future CMIP6 projections confirm precipitation's persistent dominance in drought trends, with PET contributions exhibiting regionally heterogeneous strengthening or weakening. These findings challenge warming-centric interpretations of drought trends and call for explicitly constraining precipitation uncertainty in drought-risk assessments.

Introduction

Drought is a complex and high-impact natural climate hazard, threatening ecosystems, agricultural productivity, and water security worldwide (Ahmad & Kam, 2024). Unlike rapid-onset disasters, drought is a creeping phenomenon characterized by a prolonged moisture deficit, with impacts cascading through meteorological, agricultural, hydrological, and socioeconomic systems (Mishra & Singh, 2010). Accurately defining and monitoring drought evolution remains a major scientific challenge due to its multivariate nature and the complex interplay of atmospheric and land-surface processes (Alahacoon & Edirisinghe, 2022; Liu et al., 2016). While numerous studies report that anthropogenic climate change is exacerbating land aridity and meteorological and hydrological drought risks globally (Gebrechorkos et al., 2025; Liu et al., 2024; Gu et al., 2023; Cook et al., 2018; Fu & Feng, 2014), debates on global dryland expansion (known as the "aridity paradox") have intensified in recent years (Kim et al., 2023; Berg & McColl, 2021; Greve et al., 2019; Roderick et al., 2015; Sheffield et al., 2012), particularly when drought is assessed from an ecohydrological perspective (Berg & McColl, 2021; Yang et al., 2019). In this context, accurate quantification of long-term drought trends is critically important for climate adaptation (Sun et al., 2025; Vicente-Serrano et al., 2022). Reliable drought trend assessments are essential for informing water resource management, agricultural adaptation strategies, early warning systems, and ultimately mitigating drought impacts in vulnerable regions worldwide.

Hundreds of drought indices have been developed to classify and monitor droughts (Han & Singh, 2023; Mukherjee et al., 2018). Among the most well-established indices used in climate research, the

Standardized Precipitation Evapotranspiration Index (SPEI) has emerged as a pivotal tool to capture drought dynamics under a warming climate (Vicente-Serrano et al., 2010). SPEI quantifies the climatic water balance—the difference between precipitation and potential evapotranspiration (PET)—and then standardizes it over time. This design allows SPEI to reflect not only moisture supply deficits but also the influence of increased atmospheric moisture demand associated with warming on drought severity. Consequently, SPEI-based analyses have become an important component of global drought assessments. A growing body of literature applying SPEI has suggested an apparent intensification of drought conditions in many regions over recent decades (Mwinjuma et al., 2026; Kenawy et al., 2025; Wang et al., 2018), a trend often linked to warming-induced amplification of the atmospheric evaporative demand (Gebrechorkos et al., 2025).

Despite its widespread adoption, the reliability of SPEI-based drought trend assessments is fundamentally contingent on critical but often overlooked sources of uncertainty within its input data (Hoffmann et al., 2020; Huang et al., 2026) and PET algorithms (Zhou & Yu, 2024; Zhou & Yu, 2025a). The uncertainty in SPEI calculations originates, first, from the diversity and large discrepancies among global meteorological datasets. For key inputs like precipitation, a wide array of products exist—including gauge-based, satellite-retrieved, and reanalysis data sets (Rajulapati et al., 2020; Sun et al., 2018; Gehne et al., 2016). Annual precipitation estimates over global land varied by up to 300 mm/yr among the different products (Sun et al., 2018). These datasets exhibit substantial differences in their final gridded values due to fundamental variations in source observations, spatial interpolation algorithms, the underlying physics of reanalysis models, and bias correction methods (Xiang et al., 2021; Tan et al., 2020; Sun et al., 2018). While precipitation directly defines the moisture supply, other climate variables such as temperature, radiation, and wind speed are also crucial for estimating PET. Therefore, discrepancies in these variables introduce a secondary layer of uncertainty that propagates through the PET calculation (Wang et al., 2017). Consequently, the choice of a specific meteorological dataset can significantly alter both the supply and demand sides of the climatic water balance, introducing uncertainty into the computed SPEI and the resulting drought trend signals. Furthermore, the calculation method of PET itself suffers from profound ambiguity. Different PET formulations embody distinct physical assumptions, climatic sensitivities, and data requirements (Mukherjee et al., 2018; Xiang et al., 2020). Temperature-based PET formulations such as Thornthwaite can overstate warming-induced drying in some drought-index applications, whereas PET formulations based on water balance or energy budget frameworks provide more reliable estimations (Mukherjee et al., 2018). However, even the widely used Penman and Penman-Monteith types of PET are found to overestimate evapotranspiration demand (Tang & McColl, 2025; Kim et al., 2023; Greve et al., 2019; Milly & Dunne, 2016) and land aridity trends (Zhou & Yu, 2024; Zhou et al., 2022). Recently, a number of energy-based PET formulations have been developed, considering energy constraints on evaporation over wet surfaces and land-atmosphere feedback effects, which provide a more robust representation of surface energy and water balances under warming, aligning better with observed ecohydrological changes (Tang & McColl, 2025; Zhou & Yu, 2025b; Zhou & Yu, 2024; Kim et al., 2023).

Recent sensitivity studies revealed that the selection of PET algorithms can change not only the magnitude but also the direction of inferred drought trends (Zhou & Yu, 2025b; Zhou & Yu, 2024; Yang & Roderick, 2019; Milly & Dunne, 2016; Greve et al., 2019). This means that conclusions about regional or global drying or wetting can be largely contingent on data and methodological choice, and drought trend estimates should be interpreted alongside forcing and methodological uncertainty. Consequently, the true uncertainty range and robustness of reported global drought trends—including claims of "increasing trend in drought severity worldwide" (Gebrechorkos et al., 2025) and "global drought amplification" (OECD, 2025; Ogunrinde et al., 2026)—remain poorly constrained. A comprehensive, global-scale assessment on how dataset selection interacts with PET methodology in shaping calculated SPEI trends is critically needed.

Although precipitation is often expected to be a major source of drought-index uncertainty, its relative importance and the extent to which it dominates other sources of uncertainty have not been systematically quantified at the global scale. Previous studies have shown that SPEI variability and trends are generally more sensitive to precipitation than to PET (Tomas-Burguera et al., 2020; Beguería et al., 2014; Vicente-Serrano et al., 2010), and that uncertainties in precipitation forcing can strongly affect drought assessments (Trenberth et al., 2014; Vicente-Serrano et al., 2022). However, this conceptual understanding has not yet been translated into a comprehensive quantitative evaluation of how structural uncertainties propagate from meteorological forcing and PET formulation choices into global drought trend estimates. While recent studies have begun to quantify these uncertainties at regional scales (Huang et al., 2026; Tan et al., 2023; Wang et al., 2021b; Borona et al., 2021; Shi et al., 2020), a globally consistent, multi-product, multi-timescale, and multi-PET-method evaluation remains lacking. At the global scale, several studies have compared different drought indices and their trends (Liu et al., 2024; Asadi Zarch, 2022; Vicente-Serrano et al., 2022; Trenberth et al., 2014; Dai, 2013; Sheffield et al., 2012), yet these studies have focused primarily on the resulting drought patterns or index behavior, rather than explicitly decomposing the magnitude, hierarchy, and sources of structural uncertainty in drought estimation itself. Consequently, the spatial footprint, temporal-scale dependence, and variance attribution of precipitation- and PET-related uncertainties remain unresolved.

Furthermore, separating forced signals, model uncertainty, and internal variability has a long precedent in climate uncertainty partitioning (Hawkins & Sutton, 2009). More importantly, under continued warming in the 21st-century, a critical ecohydrological question emerges: will the increasing thermodynamic forcing associated with rising atmospheric demand eventually exceed precipitation-related contributions to become the primary physical driver of drought trends? Exploring this evolving balance between precipitation-related and PET-related controls (Scheff & Frierson, 2014; Seager et al., 2010) requires a unified quantitative framework that links historical uncertainty partitioning with future projections. It necessitates a mathematically rigorous attribution framework that not only partitions historical observational uncertainties but also extends into future climate projections (e.g., CMIP6) to project the shifting geographical dominance of these physical drivers.

To address these gaps, this study provides a global quantification of structural uncertainties (data source and PET formulation discrepancies) in SPEI-based drought trends and physical attribution of drought trends (contributions of precipitation and PET changes to long-term SPEI trends). Using a 240-member factorial historical ensemble and a 72-member CMIP6 projection ensemble (see details in Methods), we aim to: (1) quantify how precipitation-product choice affects historical SPEI trend estimates; (2) decompose the structural variance in SPEI contributed by data sources and PET formulations using a nested Analysis of Variance (ANOVA); (3) disentangle the underlying physical drivers of actual SPEI trends and quantify the relative contributions of precipitation and PET variabilities across multiple accumulation timescales; and (4) assess how these contributions may shift under late-21st-century warming compared to present. This comprehensive analysis framework provides uncertainty bounds for both historical drought assessment and future drought-risk interpretation, while clarifying the respective roles of changes in precipitation and atmospheric evaporative demand.

Results

Diverging global drought trends

To assess the global trajectory of drought, we first examined the ensemble mean time series of the 240 SPEI-6 members over the historical period (1981 to 2024). To reduce instability in SPEI fitting and trend estimation over very dry or high-latitude regions, we constrained the spatial average to grid cells with annual precipitation ≥ 180 mm within 50°S–50°N (hereafter referred to as quasi-global). The resulting ensemble-mean time series exhibits a statistically significant quasi-global drying trend of − 0.0029 ± 0.0004 yr^{-1} ($P < 0.05$) from 1981 to 2024 (Fig. 1a). This ensemble-mean drying is directionally consistent with recent assessments (Gebrechorkos et al., 2025), but the robustness of this apparent trend must be evaluated against the much larger ensemble spread caused by structural uncertainties in forcing data and PET methodologies across ensemble members.

Our analysis reveals that the ensemble aggregate signal masks profound structural uncertainties inherent in the meteorological forcing data. As illustrated by the distribution of the 240 individual quasi-global trends (Fig. 1b), the mean trend of all ensemble members is − 0.0029 yr^{-1}, with a large inter-member standard deviation of ± 0.0052 yr^{-1}. Because the Sen slope was estimated separately for each member, the mean of member-level slopes in Fig. 1b (− 0.00288 yr^{-1}) differs slightly from the Sen slope fitted to the ensemble-mean time series in Fig. 1a (− 0.00292 yr^{-1}). As both values are rounded to − 0.0029, they are both referred to as ensemble-mean quasi-global trend. However, it is crucial to distinguish between the uncertainty metrics of these two calculation methods: for the ensemble-mean trend in Fig. 1a, the standard deviation of ± 0.0004 represents the statistical uncertainty in estimating the Sen's slope from the 44-year ensemble-mean time series; for the ensemble-mean trend in Fig. 1b, the substantially higher standard deviation of ± 0.0052 explicitly reflects the large structural uncertainty among the 240 SPEI ensemble members. The individual member trends span a substantial spectrum, ranging from strong negative trends (− 0.0146 yr^{-1}) to positive trends (+ 0.0080 yr^{-1}), with numerous

member confidence intervals spanning zero. Although the ensemble mean (− 0.0029 yr^{-1}) is statistically distinguishable from zero ($P < 0.001$ with a one-sample t-test of the 240 individual member trends), the sign of individual member trends is highly sensitive to precipitation-product choices: 11 members show non-significant trends (Sen slope's $P > 0.05$), 73 members exhibit significant positive (wetting) trends, and 156 members exhibit significant drying trends (see more below).

A systematic breakdown of this 240-member spread reveals that the choice of precipitation dataset constitutes the primary driver of SPEI trend uncertainty. This structural dependency is evident when the ensemble is grouped by data source or PET methods. SPEI time series aggregated by the 10 precipitation datasets (Supplementary Fig. 1) successfully capture major interannual fluctuations, reflecting a general consensus on short-term climate variability, but they diverge markedly in their long-term trends. In contrast, time series grouped by the 6 PET methods (Supplementary Fig. 2) and the 4 PET data sources (Supplementary Fig. 3) exhibit highly congruent long-term trajectories. This divergence among precipitation-grouped time series translates directly into the statistical distribution of the calculated trends. When categorizing the quasi-global SPEI trends by PET data sources and calculation methods (Fig. 1c, d, Supplementary Table 2), large intra-group spreads persist across all PET categories. Specifically, the standard deviations within individual PET source and method groups remain exceptionally high (averaging ~ 0.0049 yr^{-1}), while their group means (ranging from − 0.0056 to − 0.0002 yr^{-1}; Fig. 1c, d) vary much less than the precipitation-group means (ranging from − 0.0106 to +0.0028 yr^{-1}; Fig. 1e), indicating that PET grouping explains relatively little of the inter-member divergence in SPEI trend direction.

While grouping the results by precipitation datasets highlights the large spread of precipitation-dependent mean SPEI trends, it substantially reduces the intra-group variance (average standard deviation dropping to ~ 0.0028 yr^{-1}; Fig. 1e, Supplementary Table 2). This structural dependency is comprehensively analyzed in a suite of precipitation-specific sub-ensembles (Supplementary Fig. 4), which demonstrate that while transitioning between the 24 PET combinations under a fixed precipitation forcing yields minimal trend fluctuations, changing the precipitation product markedly shifts the baseline trend. For instance, sub-ensembles with MSWX100 (− 0.0106 ± 0.0022 yr^{-1}) and ERA5_Land (− 0.0105 ± 0.0021 yr^{-1}) precipitation products produce strong negative quasi-global SPEI trends, whereas sub-ensembles incorporating CHIRPS (+ 0.0017 ± 0.0036 yr^{-1}) or PRECL (+ 0.0028 ± 0.0037 yr^{-1}) products yield positive quasi-global SPEI trends. Furthermore, a comprehensive heatmap of all 240 SPEI trend estimates and their statistical significance (Supplementary Fig. 5) provides clear illustration for this pattern: distinct vertical banding (precipitation-driven variations) is more prominent than the weaker PET-related horizontal structure (PET-driven variations), further substantiating that the fundamental direction and significance of global drought trends are strongly conditioned by the chosen precipitation product.

To quantify the contributions of different sources to SPEI trend uncertainty, we employed a nested Type-I ANOVA to decompose the total variance of the quasi-global SPEI trends (Fig. 1f). This hierarchical framework stratifies the uncertainties into primary conceptual categories—specifically,

observation/remote-sensing versus reanalysis precipitation products, and Penman-based versus energy-based PET formulations—before evaluating individual member variations. The decomposition indicates that precipitation drives the overall uncertainty budget, accounting for a dominant 71.5% of the total variance in SPEI trends. Within this dominant factor, systematic differences between observation/remote-sensing and reanalysis precipitation products contribute 28.4%, while variations among individual precipitation datasets contribute 43.2%. Within the 240-member factorial ensemble design, PET-related uncertainty is secondary. PET calculation methods and PET data sources contribute only 12.7% and 10.7%, respectively (with the bulk of the PET method uncertainty, 12.3%, stemming from the structural divergence between Penman-based and energy-based formulations). To ensure that this result was not an artifact of the sequential nature of Type I ANOVA, we further performed a crossed three-factor ANOVA using Type I, Type II, and Type III sums of squares. The three ANOVA formulations produced identical variance fractions because of the balanced factorial ensemble design, confirming that the precipitation data uncertainty dominates SPEI trend uncertainty (Supplementary Text 2, Supplementary Table 3). Importantly, this precipitation dominance persists across varying spatial domains, precipitation mask thresholds, and temporal scales (reference time period in SPEI algorithm) (see details in Supplementary Text 3, Supplementary Figs. 6, 8).

Regional patterns of drought trends

While the global mean trend analysis identified precipitation as the dominant source of uncertainty, we further examined the spatial distribution of this precipitation dominance using the spatially resolved SPEI-6 trends derived from the 240-member multi-product ensemble (Fig. 2). The grid-level ensemble mean (Fig. 2a) reveals a spatially heterogeneous pattern of wetting and drying. Based on the aggregated regional statistics bounded by the 180 mm threshold within 50°S–50°N (Fig. 2d), South America shows the strongest regional mean drying trend among the analyzed regions (− 0.0116 yr^{-1}). Pronounced drying signals are also evident across Africa (− 0.0041 yr^{-1}) and Australia (− 0.0038 yr^{-1}). Conversely, Asia shows the largest positive regional mean SPEI trend (+ 0.0060 yr^{-1}). The 5th–95th percentile inter-member uncertainty bounds, represented by the upper (Fig. 2b) and lower limits (Fig. 2c), further reveal substantial grid-level structural uncertainty. The vast discrepancy between the strongly negative lower-bound trends and positive upper-bound trends echoes the above findings based on quasi-global trends, suggesting high sensitivity of local SPEI trends to forcing-product choice.

To decompose this local uncertainty, we mapped the grid-level ensemble-mean SPEI trends separately for each of the 10 precipitation products, averaging over PET combinations (Fig. 3). The spatial maps show that the choice of precipitation product strongly affects the estimated magnitude of regional SPEI trends. For instance, SPEI estimates based on MSWX100 and ERA5_Land (Fig. 3g-h) produce strong, spatially extensive drying trends across large portions of South America and Africa, and parts of the Mediterranean, resulting in large negative quasi-global mean trends (− 0.0111 and − 0.0110 yr^{-1} for MSWX100 and ERA5_Land, respectively; see heatmap in Fig. 3k). In contrast, ensemble means based on CHIRPS and PRECL (Fig. 3d-e) substantially weaken these drying signals, introducing broad swaths of wetting trends across Africa and the Americas, shifting their quasi-global mean trends from negative to

positive (+ 0.0016 and + 0.0028 yr^{-1}, respectively). This spatially resolved divergence in SPEI trends among precipitation products demonstrates that the precipitation-driven uncertainty is not confined to the globally averaged drought trend, but is also expressed in regional trend magnitude that highlights some regions with large hydroclimatic variability.

To quantify the spatial uncertainty in SPEI trend induced by precipitation forcing, we categorized the directional consistency among the 10 precipitation-ensemble means into seven classes (based on percentage of precipitation sources that agree on the sign of the SPEI trend) for each grid cell and for each region (Supplementary Fig. 9). The quasi-global statistics (Supplementary Fig. 9b) show that 14.93% of the land area exhibits a unanimous agreement (100% consistency) on drying across all 10 precipitation products, and about 52.63% of the land area shows a majority drying agreement (> 60% consistency). In contrast, 38.48% of quasi-global land area exhibits wetting consensus (> 60% consistency). Regions classified as “inconsistent”—where neither drying nor wetting consensus exceeds the 60% (majority) consistency threshold among the 10 datasets—account for 8.87% of the quasi-global land area.

The strongest directional consistency in drying trend occurs in the Americas. Areas with high drying consistency across the precipitation products include southern South America, the western United States, and parts of western Europe. Conversely, Asia contains the largest proportion of land area (~ 67%) exhibiting robust and high-consistency (> 60%) wetting trends across precipitation products, particularly over South and Southeast Asia (Supplementary Fig. 9). Similar high-consistency wetting signals are also evident in the eastern United States. In contrast, Africa shows the highest sensitivity to precipitation-product choice, as indicated by the largest proportion of land area (12.3%) classified as inconsistent (< 60% agreement in SPEI trend signs among the 10 precipitation datasets), which is possibly associated with sparse gauge coverage and retrieval/reanalysis differences across parts of Africa (Coz & Giesen, 2020; Kidd et al., 2017). This pattern indicates that drought trend assessments in regions like Africa and to a notable extent, parts of Australasia and Asia, require particular caution, as their long-term SPEI trends are sensitive to the precipitation product used.

Spatially explicit structural uncertainty in SPEI trend

To spatially trace the origins of drought trend uncertainties, we performed a grid-level ANOVA decomposition for the 240-member super-ensemble (Fig. 4, Supplementary Fig. 10). The spatial maps indicate that precipitation forcing (Fig. 4a) explains the largest fraction of trend variance across most analyzed land areas, whereas PET-method (Fig. 4b) and PET-source (Fig. 4c) contributions are generally smaller. Aggregating these grid-level variance contributions to regional scales (Fig. 4d) further illustrates this dominance: over the quasi-global domain, precipitation accounts for an average of 78.1% of the total variance in SPEI trends. This dominance is particularly strong in South America and Asia, where precipitation explains 85.9% and 78.9% of SPEI trend variance, respectively. Even in regions with denser observational coverage, such as Europe, precipitation uncertainty remains the primary contributor, though its contribution slightly decreases to roughly 68.0%.

The latitudinal zonal means embedded alongside the spatial maps provide critical nuance to this global picture. Throughout the 50°S to 50°N transect, the zonal mean contribution of precipitation consistently fluctuates at high levels (averaging 78.6%, peaking at over 91.6% in specific latitudinal bands). Interestingly, the minor variance contributions from PET methods (global average: 6.5%) and PET data sources (global average: 8.4%) are not uniformly distributed. The zonal profiles reveal that PET-induced uncertainties slightly amplify in certain subtropical and mid-latitude transitional zones (reaching up to ~ 13–15% locally), likely reflecting regions where aerodynamic and radiation-driven variations in different PET algorithms (e.g., Penman-based vs. energy-based) become more pronounced under specific land-atmosphere coupling conditions. However, even in these local hotspots, PET-related uncertainty in SPEI trend remains smaller than precipitation-related uncertainty.

To test whether precipitation dominance depends on the mix of precipitation-product types, we repeated the spatial ANOVA decomposition across four distinct precipitation subsets: gauge-only (Supplementary Fig. 11), satellite-only (Supplementary Fig. 12), reanalysis-only (Supplementary Fig. 13), and a strictly coupled reanalysis ensemble (where precipitation and PET are derived from the same model to preserve physical consistency; Supplementary Fig. 14). For gauge-based observations, standard reanalysis-only products and strictly coupled reanalysis products, precipitation continues to dictate the SPEI trend uncertainty, explaining an overwhelming 64.8%, 76.6%, and 89.5% of the variance (averaged over the quasi-global domain), respectively. However, for the satellite-derived precipitation subset (Supplementary Fig. 12), only two products (CHIRPS-V2 and MSWEP) are included; this reduced diversity strongly constrains the variance attributable to precipitation products. As a result, the spatially averaged contribution of precipitation decreases to 45.8% (still the dominant source), while the relative contributions of PET source (23.4%) and PET method (16.6%) become more visible across widespread regions. This subset analysis demonstrates that while precipitation is the primary source of structural uncertainty in multi-source drought assessments, the relative sensitivity of SPEI trend to PET data source and formulations becomes magnified when the diversity of precipitation forcing is strongly constrained. We also examined the influences of spatial averaging procedure, domain expansion (whether high-latitude regions are included or not) and SPEI accumulation timescale (from SPEI-1 to SPEI-24) and a leave-one-precipitation-out test on the uncertainty attribution (Supplementary Text 4; Supplementary Figs. 15–19 and 37). The results consistently show that precipitation data sources dominate the structural uncertainty of SPEI trends locally and globally.

Physical drivers of drought trends

While the above sections showed that precipitation products dominate the structural uncertainty in SPEI trends, we further examined whether actual precipitation changes — distinct from data-source uncertainty — also dominate the physical drivers of observed SPEI trends. To determine the relative physical contributions of precipitation (RC_P) and atmospheric demand (RC_{PET}) to SPEI trends at each grid cell, we employed three complementary attribution frameworks: the counterfactual scenario analysis (Scenario for short), covariance-based sensitivity analysis (Covariance), and machine learning regression (XGBoost) (see Methods “Attribution of SPEI Trends”).

All three attribution methodologies consistently identify precipitation as the dominant physical contributor to long-term SPEI trends across most of the analyzed quasi-global land area (Fig. 5a, c, e). The quasi-global average RC_P is consistently dominant across all three methods (Fig. 5g-i): 74.6% (Scenario), 66.9% (Covariance), and 66.0% (XGBoost), with RC_{PET} explaining the remaining fraction (< 35%). The frequency distributions of the relative contributions across global grid cells reveal that the Scenario and XGBoost methods identify more concentrated RC_P values around the mean, whereas the Covariance method identifies a wider spread but a higher peak RC_P, with their mean and median values all exceeding 65% (Supplementary Fig. 20). Even in many rapidly warming regions, precipitation remains the larger contributor to historical SPEI trends. The geographic core zones of precipitation dominance show strong physical consistency with the trends of input precipitation and PET fields (Supplementary Figs. 21, 22). The severe drying hotspots in Central and South America and central Africa closely correspond to regions of strongly declining precipitation, corroborating precipitation's dominant physical role.

To ensure that this precipitation dominance is not merely a statistical coincidence bound to the ensemble mean, we re-run all three attribution frameworks for each of the 10 precipitation datasets (Supplementary Figs. 23–28). The results underscore a strong cross-product consistency. Regardless of the underlying precipitation product used, the quasi-global mean RC_P remains universally larger than RC_{PET}. The Scenario method produces the largest estimates, with quasi-global RC_P ranging from 70.1% to 78.6% (Supplementary Fig. 23) across precipitation products, whereas the Covariance and XGBoost methods yield more conservative but still precipitation-dominant RC_P ranges of 59.5%–76.7% (Supplementary Fig. 24) and 59.9%–74.6% (Supplementary Fig. 25), respectively. Furthermore, the individual frequency distributions of RC_P across all three methodologies and all 10 precipitation sources consistently show mean and median values exceeding 60% (Supplementary Figs. 26–28). This indicates that precipitation remains the dominant physical contributor across the precipitation products and analytical frameworks tested here.

Going beyond regional averages, we further investigated whether these 10 precipitation datasets structurally agree on the spatial locations where precipitation physically dominates over PET in determining SPEI trends. By categorizing their internal consensus on the primary physical driver (Supplementary Figs. 29–31 for Scenario, Covariance, and XGBoost agreements), we found the spatial consensus to be remarkably robust across all three analytical frameworks. The Scenario approaches the strongest cross-source agreement. Over the 50°S–50°N domain, 34.1% of the analyzed land areas exhibit a unanimous (100%) agreement among all 10 distinct precipitation datasets that precipitation acts as the dominant driver, and 74.9% of the land area reaches at least 60% agreement. The Covariance and XGBoost approaches yield more conservative but still spatially extensive agreement, with areas reaching at least 60% cross-source consensus for precipitation dominance accounting for 54.4% and 54.3% of the quasi-global land area, respectively. Spatially, high-consensus precipitation-dominant regions are mainly distributed across large parts of North America, Europe, South and East Asia,

southeastern South America, and southern Australia, whereas inconsistent or PET-dominant signals are more evident in parts of tropical South America, Africa, and semi-arid transition zones.

While the preceding analyses demonstrate the mathematical robustness of our attribution methods for SPEI trends, we sought an additional, stringent physical cross-validation against another drought metric—the Standardized Precipitation Index (SPI)—calculated using both the full ensemble (Supplementary Fig. 32) and each of the 10 precipitation subsets (Supplementary Fig. 33). Because SPI intrinsically excludes atmospheric evaporative demand, its spatial trends provide a precipitation-only benchmark by construction. A pixel-wise spatial correlation analysis between these SPI trends and the statistically isolated signed precipitation contribution to SPEI (Supplementary Fig. 34) reveals a strong spatial alignment. The zonal mean spatial correlations (R) remain consistently positive and generally across the entire 50°S–50°N transect and across the three attribution frameworks, indicating that the precipitation component isolated from SPEI trends closely follows the independent precipitation-only drought signal. This continuous latitudinal and methodological agreement indicates that the physical consistency between different drought metrics captured by our attribution models is a pervasive global phenomenon rather than a localized artifact. This consistency supports the conclusion that precipitation changes explain the dominant share of historical SPEI trend, despite increasing PET under warming.

Persistent dominance of precipitation under escalating warming

As we transition from historical reconstructions to future CMIP6 projections, the dominant source of drought-trend uncertainty shifts. A temporal ANOVA decomposition of the 72-member CMIP6 ensemble (Supplementary Fig. 35) reveals that structural uncertainties in climatic variables (including precipitation) under future projections are overwhelmingly dictated by General Circulation Model (GCM) inter-model structural uncertainty rather than PET methodological choices. This finding aligns with established climate projection studies, which consistently identify GCM structural uncertainty as the primary source of variance in future hydroclimatic assessments (Niu et al., 2025; Wu et al., 2021; Ukkola et al., 2020). Across both the global and 50°S–50°N domains, the GCM structure consistently accounts for over 90% of the SPEI trend variance throughout the 21st century, rendering the methodological discrepancies among PET formulations practically negligible (~ 2–4%).

We then asked a separate physical question: whether rising temperature would cause atmospheric-demand to dominate over precipitation in driving SPEI trends over the 21st century? To answer this question, we used both Covariance and XGBoost methods to quantify the contributions of temporal evolution of precipitation (RC_P) and PET (RC_{PET}) to long-term SPEI trends using a 30-year moving window across the CMIP6 ensemble (Fig. 6; see Methods “Attribution of SPEI Trends”).

The temporal aggregation (1996–2086) over the quasi-global domain shows persistent precipitation dominance in driving SPEI trends over the 21st century (Fig. 6c, d). Consistent with theoretical expectations of an intensifying hydrological cycle and rising atmospheric evaporative demand, the RC_{PET} increases, reducing RC_P over time. However, this increased PET contribution does not exceed the

precipitation contribution in the quasi-global mean. Under the Covariance framework, the ensemble mean RC_P gradually declines from 61.3% in 1996 to 57.3% by 2086, while RC_{PET} increases from 38.7% to 42.7%. The XGBoost framework shows a similar tendency, with RC_P declining from 62.8% to stabilize at 56.8% and RC_{PET} increasing from 37.2% to 43.2%. This temporal resilience suggests that, within the CMIP6 ensemble analyzed here, precipitation remains the dominant contributor to long-term drought evolution at the quasi-global scale.

The latitudinal progression of RC_P over the 21st century (Hovmöller diagram in Fig. 6a, b) reveals that the warming-induced enhancement of RC_{PET} is not globally uniform. Precipitation dominance is most persistent across mid- to high-latitude regions, particularly in the Northern Hemisphere, where RC_P generally remains above 60% and is supported by strong ensemble agreement. In contrast, lower RC_P values and regions approaching or falling below the 50% threshold are mainly concentrated in tropical and subtropical latitude bands, indicating that PET-related effects become increasingly important in these hydroclimatic transition zones. This latitudinal contrast suggests that rising atmospheric evaporative demand can more strongly amplify drought trends in regions where precipitation dominance is weaker. Overall, the Hovmöller analysis confirms that future PET effects strengthen regionally rather than uniformly, but they do not overturn the dominant role of precipitation in quasi-global SPEI trend evolution.

Although the quasi-global mean remains precipitation-dominated, the spatially explicit maps of historical and future attributions (Fig. 7) unveil a regionally heterogeneous redistribution of thermodynamically-driven shift in the physical drivers of drought trends. During the historical baseline of CMIP6, quasi-global mean RC_P reaches 60.5% under the Covariance method and 61.5% under XGBoost method (Supplementary Fig. 36a), broadly consistent with the historical observation-based attribution results (Fig. 5). To quantitatively pinpoint the geographical hotspots of this thermodynamic shift, we analyzed the signed change in RC_P between the historical baseline (1996–2015) and the mid-future (2036–2055) as well as far-future projection (2066–2085). As illustrated in Fig. 7, the resulting Δ maps clearly show a spatially heterogeneous decline in RC_P, which corresponds directly to the localized increase in RC_{PET} (Supplementary Fig. 36b-e).

Future projections indicate that this PET-related increase is detectable but moderate at the quasi-global scale. Quasi-global RC_P decreases by 2.3 and 3.6 percentage points by the mid-future under the Covariance and XGBoost frameworks, respectively, with equivalent increases in RC_{PET} (Supplementary Fig. 36b, d). By the far future, the corresponding reductions in RC_P are 2.3 and 4.1 percentage points, respectively. However, the spatial extent of robust model-consistent change remains limited. Only 13.1% and 11.2% of quasi-global land grid points (Supplementary Fig. 36c, e) show robust changes by the mid-future under the Covariance and XGBoost frameworks, respectively, and these fractions increase only slightly to 15.5% and 12.4% by the far future. Regionally, the clearest PET-related strengthening occurs in Sub-Saharan Africa, Asia and Siberia, where RC_P declines most consistently across both attribution frameworks. In contrast, Europe shows a slight increase in RC_P, whereas North America exhibits only

weak changes. Overall, these projections paint a dual pattern for 21st-century drought evolution. Precipitation remains the dominant contributor to the quasi-global mean drought trend, the warming-driven increases in PET impose a localized thermodynamic contribution to drought intensification, reshaping drought mechanisms across several densely populated and hydro-climatically sensitive regions. Future PET enhancement therefore modifies regional drought attribution patterns, but does not overturn the broader precipitation-dominant regime.

Discussion

Using a 240-member SPEI super-ensemble, we find large structural uncertainty in estimated drought trends, with the inter-member spread (± 0.0052 yr^{-1}) exceeding the ensemble-mean quasi-global SPEI trend (– 0.0029 yr^{-1}) in magnitude. While the ensemble mean is statistically distinguishable from zero, the sign of individual member trends is highly sensitive to precipitation-product choices. Some observation-based ensemble subsets combining gauge- or satellite-derived precipitation with energy-based PET formulations yield non-significant quasi-global SPEI trends (11 members) or significant wetting trends (73 members). Through quantitative uncertainty analysis, we demonstrate that precipitation-product differences are the dominant source of this structural uncertainty, accounting for 71.5% of quasi-global mean and 78.1% of grid-level SPEI trend variance during 1981–2024. Our physical attribution analyses further indicate that precipitation changes explain the majority of both historical and future SPEI trends, with PET remaining a secondary contributor. Apparent drying trends in widely cited single- or few-dataset assessments are therefore strongly influenced by precipitation data choices and should not be interpreted as robust hydroclimatic signals without explicit uncertainty quantification.

These findings challenge recent assessments that emphasize the role of warming-driven atmospheric evaporative demand in historical drought intensification (Gebrechorkos et al., 2025). Our results are consistent with broader evidence that precipitation remains one of the most uncertain and product-sensitive variables in global hydroclimatic assessments, particularly when gauge-based, satellite-derived, merged, and reanalysis products are compared (Mankin et al., 2025; Gebrechorkos et al., 2024; Sun et al., 2018). ERA5 illustrates this sensitivity, as it captures several key features of global precipitation change but shows weaker agreement with other precipitation products for long-term trends than for climatological means or interannual variability (Obarein & Lee, 2025). Recent evidence also suggests that ERA5_Land may produce stronger long-term drying trends than observation-constrained estimates (e.g., GLEAM) because of temporally varying precipitation biases (Wang et al., 2026). Consistently, our spatial ANOVA suggests that the stronger drying signals derived from reanalysis or hybrid products such as ERA5_Land and MSWX100 than gauge-based (CRU, GPCC, CPC, and PRECL) or satellite-derived (CHIRPS and MSWEP) products reflect structural differences in precipitation estimation, data assimilation, and product construction, rather than true drying signals (Wang et al., 2026; Sun et al., 2018).

The profound structural uncertainties inherent in precipitation datasets are highly regional, reflecting differences in rain-gauge networks, satellite retrievals, reanalysis physics, gauge correction, terrain

effects, snowfall processes, and temporal homogenization (Su et al., 2026; Mankin et al., 2025; Sun et al., 2018). Some regions with denser observational infrastructures, including parts of North America and Europe, show greater agreement in drought-trend direction, whereas data-sparse and process-complex regions, particularly parts of Africa and the Amazon basin, exhibit larger precipitation and SPEI trend divergence. A recent study shows that only 13.4% of the global land surface currently meets WMO requirements for annual precipitation monitoring, with acute gaps in many low-latitude, high-latitude, and socioeconomically vulnerable regions (Su et al., 2026). Reducing precipitation observational uncertainty, through denser in-situ station networks and better-calibrated satellite missions, therefore remains central to improving both historical drought assessment and future drought-risk projection (Su et al., 2026; Mankin et al., 2025; Gebrechorkos et al., 2024; Sun et al., 2018).

Looking ahead to the late-21st -century CMIP6 projections, our results reveal a spatially heterogeneous shift in the drivers of global SPEI evolution. While precipitation remains the larger contributor to quasi-global SPEI trends, PET-related contributions increase regionally, especially in some tropical, subtropical, and hydroclimatic transition zones such as sub-Saharan Africa and Asia (including China and India) where precipitation control weakens (Fig. 7). The shift toward stronger PET control in these hotspots is broadly consistent with regions where recent studies have identified elevated flash-drought risk under warming triggered by extreme temperature anomalies and intensified atmospheric demand together with precipitation-deficit episodes through land–atmosphere coupling (Yuan et al., 2023; Christian et al., 2021; Otkin et al., 2018; Seneviratne et al., 2010). Thus, our finding of persistent precipitation dominance does not undermine the role of true atmospheric demand changes in shaping drought severity and its trend. The transition toward stronger PET-related control in these transitional zones signals a potential amplification of rapid-onset, compound heat-drought events, which may be underrepresented by monthly drought indices.

The CMIP6 projected limited increase in PET contributions to ensemble-mean quasi-global SPEI trends should be interpreted with caution. Meteorological drought indices such as SPEI use offline PET as an atmospheric-demand term, which may overstate realized terrestrial water stress in moisture-limited regions due to neglection of land-surface constraints (Beguería et al., 2014; Vicente-Serrano et al., 2010). In moisture-limited regimes, actual evapotranspiration is often constrained more strongly by water supply than by atmospheric demand (Berg & McColl, 2021; Roderick et al., 2015). Furthermore, it is increasingly known that Penman- and Penman-Monteith types of PET formulation may overestimate future increases in evaporation demand due to their ignorance of critical land–atmosphere feedbacks when a dry surface becomes wet (Kim et al., 2023; Zhou & Yu, 2024; Tang & McColl, 2025) and the physiological effects of elevated CO_2 on stomatal conductance and vegetation water-use efficiency (Milly & Dunne, 2016; Swann et al., 2016). The net ecohydrological response to rising CO_2 depends on vegetation structure, leaf-area changes, rooting depth and soil moisture availability (Mankin et al., 2019; Yang et al., 2019). Without considering these feedbacks, future PET-based drought severity may be overstated, particularly in arid and semi-arid regions (Zhou & Yu, 2025b; Kim et al., 2023). To address this limitation, recent studies have developed several energy-based PETs which explicitly incorporate land-atmosphere coupling mechanisms (see ZY, YA, MD and KIM algorithms in Supplementary Text 1). That’s

why the sub-ensembles calculated with Penman-based PETs show negative quasi-global SPEI trends (drying), whereas the sub-ensembles calculated with energy-based PETs show negligible trends (Fig. 1d). Therefore, the projected limited increase of PET-related contribution should at best be interpreted as an upper-bound estimate of atmospheric-demand stress.

Our findings have strong implications for the ecohydrological interpretation of PET-based drought metrics (Greve et al., 2014; Roderick et al., 2007). The apparent tension between an intensified global hydrological cycle with regionally heterogeneous precipitation changes (Douville et al., 2021; Allan et al., 2020; Chen et al., 2020; Held & Soden, 2006) and previous SPEI-based estimates of drought intensification (Gebrechorkos et al., 2025) is largely attributed to precipitation-product choices, and also partly linked to the limitations of offline empirical PET formulations as proxies for terrestrial water stress as shown above. Other studies also show that projected drought changes vary substantially across hydroclimatic variables and drought metrics, including precipitation, soil moisture, runoff, and PET-based indices (Cook et al., 2020; Zhao & Dai, 2022). To resolve this tension, drought trend assessments should move away from simple empirical indices towards more robust physical models (McColl et al., 2022).

Future drought assessments should therefore complement standardized offline indices with coupled Earth System Model diagnostics and systematic observations of soil moisture, runoff, evapotranspiration, and vegetation physiological responses, rather than treating index-based and process-based metrics as interchangeable (Ukkola et al., 2020; Cook et al., 2020; Berg et al., 2016). Advancing future drought assessment and projection requires both improved multi-source regional precipitation monitoring networks (Su et al., 2026; Wang et al., 2023) and greater integration of physically based, holistic hydrological assessment frameworks that represent land-surface and vegetation feedbacks (Zhou & Yu, 2025b; Kim et al., 2023; Milly & Dunne, 2016). Ultimately, future drought evolution is unlikely to be explained by a uniform thermodynamic drying mechanism alone; rather, it will reflect spatially heterogeneous interactions among precipitation variability, atmospheric demand, land-surface constraints, and vegetation responses.

Methods

Drought index and climate datasets

A widely utilized drought index, SPEI, that incorporates both precipitation and atmospheric evaporative demand (PET) was employed to evaluate global drought severity. The SPEI is computed by standardizing the precipitation-minus-PET difference through a log-logistic distribution, with its parameters (α, β, γ) estimated by the L-moment method, to ensure spatiotemporal comparability. We employed the entire period from 1981 to 2024 as the baseline for SPEI calculation to capture the full variability inherent in the input data. SPEI was computed using the R package available on GitHub at https://github.com/sbegueria/SPEI/. Our core analysis centered on the 6-month SPEI, which strikes an optimal balance between capturing short-term meteorological anomalies and reflecting emerging intermediate-term hydrological trends (Gebrechorkos et al., 2025; Zhou et al., 2025; Wang et al., 2021a).

A full-spectrum multi-scale sensitivity assessment was also conducted across 1- to 24-month timescales (SPEI-1, 3, 12, and 24). To ensure temporal consistency across all timescales (accounting for the 24-month data spin-up required for SPEI-24), this multi-scale evaluation was constrained to a common analysis period of 1983–2024 to accurately investigate temporal scaling effects and cumulative drought memory.

PET was estimated using six distinct methods: the Penman (Penman, 1948) equation for open water surfaces (Stedinger et al., 1993) (abbreviated as PE-OW), the Penman-Monteith formulation (Allen et al., 1998) (abbreviated as PM), and the energy-based PET formulations of Zhou & Yu (2024) (abbreviated as ZY), Yang et al. (2019) (abbreviated as YA), Milly & Dunne (2016) (abbreviated as MD), and Kim et al. (2023) (abbreviated as KIM). Details of PET formulations were provided in Supplementary Text 1.

Four meteorological datasets, ERA5_Land (Muñoz-Sabater et al., 2021), MSWX100 (Beck et al., 2022), JRA-3Q (Kosaka et al., 2024), and MERRA-2 (Gelaro et al., 2017) were used to calculate PET for each of the six PET methods, yielding 24 distinct PET datasets. When calculating PET with the MSWX100 dataset, a few meteorological variables (e.g., sensible heat flux, latent heat flux, and skin temperature) were missing. These data gaps were filled using the corresponding records from the ERA5_Land dataset.

Utilizing precipitation data from ERA5_Land, MSWX100, JRA-3Q, MERRA-2, and additionally MSWEP (Beck et al., 2019), CHIRPS (Funk et al., 2015), CRU (Harris et al., 2020), CPC (Xie et al., 2010), GPCC (Schneider et al., 2008), and PRECL (Chen et al., 2002), we performed a full factorial combination of 10 precipitation datasets with 24 PET datasets, yielding a massive historical super-ensemble of 240 SPEI datasets. Details of the data used in this study are summarized in Supplementary Table 1. We used monthly data from all meteorological datasets. The original spatial resolutions of these datasets range from 0.05°×0.05° to 0.5° × 0.5°. To construct the SPEI super-ensemble, they were spatially aligned to a consistent 0.5° × 0.5° (latitude 180 × longitude 360) resolution through interpolation or resampling.

To project future drought trajectories and attribute their physical drivers under escalating warming, we further incorporated climate projections from 13 Earth System Models participating in CMIP6 (Coupled Model Intercomparison Project Phase 6). The selected models include ACCESS-CM2, AWI-CM-1-1-MR, BCC-CSM2-MR, CMCC-CM2-SR5, EC-Earth3, GFDL-ESM4, IITM-ESM, KACE-1-0-G, KIOST-ESM, MIROC-ES2L, MIROC6, MPI-ESM1-2-HR, and MRI-ESM2-0. For each model, we utilized outputs from the Historical experiment (1980–2014) combined with the high-emission Shared Socioeconomic Pathway (SSP5-8.5) extending to the late 21st century (2015–2099). To ensure physical consistency and mitigate systematic model biases, all CMIP6 outputs were first interpolated to a common 1° × 1° spatial resolution, and subsequently rigorously post-processed using a bias and variance correction approach (Fan & McColl, 2024) before calculating future SPEI.

Drought trend

The long-term trends in SPEI were analyzed using the non-parametric Mann-Kendall test and Sen's slope estimator. For each pixel, the Mann-Kendall test detects the statistical significance of monotonic trends,

while Sen's slope estimator quantifies the magnitude of change by computing the median of all pairwise slopes. This combined approach provides a robust measure of trend direction and rate, resistant to outliers and non-normal data distributions.

To ensure consistency with the spatial coverage of CHIRPS, which is available only between 50°S and 50°N, the quasi-global mean SPEI time series was computed over land areas within this latitude band. Grid cells with long-term mean annual precipitation below 180 mm were further excluded, in a similar way to Gebrechorkos et al. (2025), to avoid unstable SPEI estimates in extremely dry regions, where the P – PET distribution is highly skewed and SPEI trends can become overly sensitive to PET formulation choices rather than meaningful hydroclimatic variability. Sensitivity tests (Supplementary Text 3, Supplementary Fig. 6) using alternative spatial domains (quasi-global vs. global) and precipitation mask thresholds of 100 and 250 mm showed that the ANOVA-based uncertainty decomposition was robust to the domain and precipitation mask choices. To rigorously verify the physical dominance of precipitation and provide a pure thermodynamic-free baseline, the Standardized Precipitation Index (SPI) was concurrently computed. Spatial correlations between actual SPI trends and the statistically isolated precipitation contributions to SPEI were calculated for independent physical cross-validation. To display global spatial distributions, the maps combine data from different sources. For the 50°N–50°S region, a composite of all 10 precipitation sources is used. Areas poleward of 50°N and 50°S are represented using a composite of 9 global precipitation sources (excluding CHIRPS).

Uncertainty Analysis

To systematically quantify the uncertainties cascading from different data inputs, model simulations, and methodological choices, a multi-tiered Analysis of Variance (ANOVA) (Stahle & Wold, 1989) framework was implemented. This framework disentangles the total variance in long-term SPEI trends at both the localized pixel level and the aggregated regional macro-scale. All variance decompositions were executed using ordinary least squares (OLS) regression models and Type I (sequential) ANOVA, which calculates the relative fractional contribution of each factor as the ratio of its sum of squares to the total sum of squares (SST).

To preserve local spatial heterogeneity and identify regional uncertainty hotspots, a pixel-by-pixel ANOVA was first conducted across the global grid (0.5° × 0.5°). For the historical observation-based ensemble, a three-way ANOVA was applied to partition the variance into three independent sources: the choice of precipitation dataset, the choice of meteorological dataset used for PET forcing, and the choice of PET calculation method. To account for the spatial limitations of the CHIRPS dataset, the degrees of freedom for the precipitation factor were dynamically adjusted for regions poleward of 50°N/S. For the CMIP6 future projection ensemble, a corresponding two-way ANOVA was executed to isolate the structural variance between the climate models and the PET methodologies. The total trend variance in this coupled framework was partitioned into the choice of the Earth System Model and the PET calculation method.

Furthermore, to unveil profound spatial scaling effects and investigate how specific conceptual categories of datasets and methods drive uncertainty, a nested hierarchical ANOVA was performed on pre-aggregated regional and global mean time-series trends. Aggregating the data acts as a spatial low-pass filter, muting local chaotic noise to reveal foundational methodological divergences. Unlike the standard pixel-wise approach, this time-series ANOVA utilized a highly disaggregated five-factor nested structure. Specifically, the total variance was partitioned into: (1) fundamental precipitation type, capturing the fundamental divergence between observation/satellite-blended products and atmospheric reanalysis models; (2) precipitation source, capturing the internal differences among individual datasets within the same precipitation type; (3) PET data source, representing the uncertainty introduced by the background meteorological forcing; (4) PET method type, capturing the fundamental thermodynamic divergence between traditional aerodynamic formulations (Penman-based) and physically constrained energy-based formulations; and (5) PET method, capturing the minor internal algorithmic differences within the same PET category. By systematically comparing the nested time-series ANOVA with the pixel-wise ANOVA, this dual-framework robustly isolates whether drought trend uncertainties are driven by localized observational noise or by fundamental, systemic biases in hydroclimatic methodologies.

Attribution of SPEI Trends

To comprehensively disentangle and quantify the individual drivers of long-term SPEI trends, we employed a robust multi-method attribution framework. The individual contributions of precipitation (P) and PET were cross-validated using the following three independent analytical approaches:

Counterfactual scenario analysis. Following a method similar to Gebrechorkos et al. (2025), the contributions were determined by calculating the difference between the observed SPEI trends and trends derived from counterfactual climatological scenarios. The absolute trend contribution of PET (C_{PET}) and precipitation (C_P) were defined as:

$$C_{PET} = T_{obs} - T_{P_obs,PET_clm} \text{ (Eq. 1)}$$

$$C_P = T_{obs} - T_{P_clm,PET_obs} \text{ (Eq. 2)}$$

where T_{obs} is the SPEI trend calculated with observed precipitation and PET. T_{P_obs,PET_clm} is the trend driven by observed precipitation but holding PET at its climatological mean, and vice versa for T_{P_clm,PET_obs}. The relative percentage contribution (RC_P) of each factor was then calculated to provide a standardized measure of influence:

$$RC_P = \frac{|C_P|}{|C_P|+|C_{PET}|} \times 100 \text{ (Eq. 3)}$$

Covariance-based sensitivity analysis. To capture the physical sensitivity of SPEI to its climatic drivers, we calculated the sensitivity coefficients (β_P) based on the variance ($var(PET)$, $var(P)$) and covariance ($cov(SPEI, P)$, $cov(P, PET)$, $cov(SPEI, PET)$) of the historical time series. The sensitivity of SPEI to precipitation (β_P) was formulated as:

$$\beta_P = \frac{var(PET)\cdot cov(SPEI,P) - cov(P,PET)\cdot cov(SPEI,PET)}{var(P)\cdot var(PET) - cov(P,PET)^2} \quad \text{(Eq. 4)}$$

The long-term trend contribution was then obtained by multiplying the derived sensitivity coefficient by the observed linear trend of the respective climate variable:

$$RC_P = \frac{|\beta_P \times Trend_P|}{|\beta_P \times Trend_P| + |\beta_{PET} \times Trend_{PET}|} \times 100\% \quad \text{(Eq. 5)}$$

Machine learning and SHAP interpretation. To account for non-linear and non-stationary interactions between climate drivers, a machine learning approach was also implemented to quantify precipitation and PET contributions to SPEI trends. For each valid land pixel, an Extreme Gradient Boosting (XGBoost) regression model was trained to predict SPEI using precipitation and PET time series as predictors. TreeExplainer from the SHapley Additive exPlanations (SHAP) framework was then applied to extract the independent marginal contribution of each variable at every time step. The contributions of precipitation and PET to long-term SPEI trend were estimated from the temporal trends of their corresponding SHAP components. Specifically, the contribution of precipitation was calculated as the long-term trend of the precipitation-related SHAP component, while the PET contribution was calculated analogously from the PET-related SHAP component. The relative contribution of precipitation to the SPEI trend was then defined as:

$$RC_P = \frac{|Trend(SHAP_P)|}{|Trend(SHAP_P)| + |Trend(SHAP_{PET})|} \times 100\% \quad \text{(Eq. 6)}$$

While all three attribution frameworks were cross-validated using the historical SPEI-6 dataset, the extended CMIP6 future projections were conducted using the Covariance-based and XGBoost-SHAP approaches. The counterfactual scenario method provides an intuitive and effective baseline for historical attribution; however, its application to future climate projections requires establishing stationary climatological references. This becomes methodologically challenging under the strongly non-stationary and dynamically coupled warming trajectories of CMIP6 (e.g., SSP5-8.5), where precipitation and PET co-evolve simultaneously. In contrast, the covariance-based framework provides a physically interpretable and computationally efficient estimate of precipitation and PET contributions to SPEI trends, while the SHAP framework captures non-linear responses and interaction effects learned by XGBoost. These complementary strengths make the two approaches suitable for moving-window across large CMIP6 ensembles.

Finally, to trace the dynamic evolution of precipitation and PET contributions under future warming, the covariance-based and XGBoost-SHAP attribution frameworks were applied to the CMIP6 ensemble using a 30-year moving window, continuously advancing from 1981–2010 to 2070–2099) across the 21st century. To evaluate the reconstruction fidelity of the covariance-based and XGBoost-SHAP frameworks, we further quantified their model skill using four complementary metrics: the coefficient of determination (R^2), Pearson correlation, root mean square error (RMSE), and the absolute trend gap between reconstructed and target SPEI trends. These metrics were calculated for both the historical

ensemble and the CMIP6 future projection ensemble to assess whether the two attribution frameworks could reliably reproduce SPEI variability and long-term trends. The spatial distributions of these evaluation metrics are presented in Supplementary Figs. 38 and 39.

Software and Implementation

The computation of the grid-by-grid SPEI and SPI indices was conducted in the R programming environment, utilizing the SPEI package for standardized index calculations, alongside the ncdf4 and parallel libraries for NetCDF file operations and multi-core parallel processing. Subsequent data preprocessing, spatial alignment, and statistical modeling were executed using Python (version 3.12.11). The multi-dimensional climate datasets were manipulated and analyzed utilizing the xarray and numpy libraries. The ANOVA and statistical significance tests were implemented using the statsmodels package. For the machine learning-based attribution analysis, the Extreme Gradient Boosting algorithm and its corresponding interpretability analysis were performed using the xgboost and shap libraries, respectively. All spatial parallel computations were optimized using Python's native multiprocessing module.

Declarations

Competing Interests

The authors declare no competing interests in this study.

Author contributions

Conceptualization: YF

Acknowledgments

Y.F. acknowledges supports from Shenzhen Science and Technology Program (No. ZDSYS20220606100806014) and the Scientific Research Start-up Funds (QD2023021C) from Tsinghua Shenzhen International Graduate School. X.Z. acknowledges supports from the project of Key Laboratory of Changjiang Regulation and Protection of Ministry of Water Resources (QTKS0034W25089). We are grateful to Kaighin McColl, Alexis Berg, Sha Zhou, and Jian Yang for helpful discussions during the early stage of this study.

Data availability

All climate data described in the main text are publicly available. The MSWX100 data (version V100) are available from the GloH2O platform at https://www.gloh2o.org/mswx/. The ERA5_Land data (accessed June 2025) are available from the European Centre for Medium-Range Weather Forecasts (ECMWF) at https://cds.climate.copernicus.eu/datasets/reanalysis-era5-land?tab=overview. The JRA-3Q data (accessed May 2026) are provided by the Japan Meteorological Agency (JMA) at https://www.data.jma.go.jp/jra/html/JRA-3Q/index_en.html. The MERRA-2 data (version 2) are distributed by NASA's Global Modeling and Assimilation Office (GMAO) at https://gmao.gsfc.nasa.gov/gmao-products/merra-2/. The MSWEP precipitation dataset (version V2.8) is available from the GloH2O website at https://www.gloh2o.org/mswep/. The CRU data (version TS_V4.09) are provided by the Climatic Research Unit at https://crudata.uea.ac.uk/cru/data/hrg/cru_ts_4.09/. The CHIRPS precipitation data (version V2) are distributed by the Climate Hazards Group at https://www.chc.ucsb.edu/data/chirps/. The CPC global precipitation data (accessed May 2026) are available from the NOAA Climate Prediction Center (CPC) at https://www.psl.noaa.gov/data/gridded/data.cpc.globalprecip.html. The GPCC precipitation data (version 2025) are provided by the NOAA Physical Sciences Laboratory (PSL) at https://psl.noaa.gov/data/gridded/data.gpcc.html. The PRECL precipitation data (accessed April 2026) are available from the NOAA Physical Sciences Laboratory (PSL) at https://www.psl.noaa.gov/data/gridded/data.precl.html. The original CMIP6 climate data used in this study are available at the Earth System Grid Federation nodes (https://esgf-ui.ceda.ac.uk/search).

Code availability

The intermediate data and code for replicating the figures and analysis are available in the Figshare repository (https://figshare.com/s/cc6cfb9db14225d9b28f).

References

1. Ahmad, D. M., & Kam, J. (2024). Disparity between global drought hazard and awareness. *Npj Clean Water*, *7*(1), 75. https://doi.org/10.1038/s41545-024-00373-y
2. Alahacoon, N., & Edirisinghe, M. (2022). A comprehensive assessment of remote sensing and traditional based drought monitoring indices at global and regional scale. *Geomatics, Natural Hazards and Risk*, *13*(1), 762–799. https://doi.org/10.1080/19475705.2022.2044394
3. Allan, R. P., Barlow, M., Byrne, M. P., Cherchi, A., Douville, H., Fowler, H. J., et al. (2020). Advances in understanding large-scale responses of the water cycle to climate change. *Annals of the New York Academy of Sciences*, *1472*(1), 49–75. https://doi.org/10.1111/nyas.14337
4. Allen, R. G., Pereira, L. S., Raes, D., & Smith, M. (1998). Crop evapotranspiration-guidelines for computing crop water requirements-FAO irrigation and drainage paper 56.
5. Asadi Zarch, M. A. (2022). Past and Future Global Drought Assessment. *Water Resources Management*, *36*(13), 5259–5276. https://doi.org/10.1007/s11269-022-03304-z

6. Beck, H. E., Wood, E. F., Pan, M., Fisher, C. K., Miralles, D. G., Van Dijk, A. I. J. M., et al. (2019). MSWEP V2 Global 3-Hourly 0.1° Precipitation: Methodology and Quantitative Assessment. *Bulletin of the American Meteorological Society*, *100*(3), 473–500. https://doi.org/10.1175/BAMS-D-17-0138.1
7. Beck, H. E., Van Dijk, A. I. J. M., Larraondo, P. R., McVicar, T. R., Pan, M., Dutra, E., & Miralles, D. G. (2022). MSWX: Global 3-Hourly 0.1° Bias-Corrected Meteorological Data Including Near-Real-Time Updates and Forecast Ensembles. *Bulletin of the American Meteorological Society*, *103*(3), E710–E732. https://doi.org/10.1175/BAMS-D-21-0145.1
8. Beguería, S., Vicente-Serrano, S. M., Reig, F., & Latorre, B. (2014). Standardized precipitation evapotranspiration index (SPEI) revisited: Parameter fitting, evapotranspiration models, tools, datasets and drought monitoring. *International Journal of Climatology*, *34*(10), 3001–3023. https://doi.org/10.1002/joc.3887
9. Berg, A., & McColl, K. A. (2021). No projected global drylands expansion under greenhouse warming. *Nature Climate Change*, *11*(4), 331–337. https://doi.org/10.1038/s41558-021-01007-8
10. Berg, A., Findell, K., Lintner, B., Giannini, A., Seneviratne, S. I., Van Den Hurk, B., et al. (2016). Land–atmosphere feedbacks amplify aridity increase over land under global warming. *Nature Climate Change*, *6*(9), 869–874. https://doi.org/10.1038/nclimate3029
11. Borona, P., Busch, F., Krueger, T., & Rufin, P. (2021). Uncertainty in Drought Identification Due to Data Choices, and the Value of Triangulation. *Water*, *13*(24), 3611. https://doi.org/10.3390/w13243611
12. Chen, M., Xie, P., Janowiak, J. E., & Arkin, P. A. (2002). Global land precipitation: a 50-yr monthly analysis based on gauge observations. *Journal of Hydrometeorology*, *3*(3), 249–266. https://doi.org/10.1175/1525-7541(2002)003%3C0249:GLPAYM%3E2.0.CO;2
13. Chen, Z., Zhou, T., Zhang, L., Chen, X., Zhang, W., & Jiang, J. (2020). Global Land Monsoon Precipitation Changes in CMIP6 Projections. *Geophysical Research Letters*, *47*(14), e2019GL086902. https://doi.org/10.1029/2019GL086902
14. Christian, J. I., Basara, J. B., Hunt, E. D., Otkin, J. A., Furtado, J. C., Mishra, V., et al. (2021). Global distribution, trends, and drivers of flash drought occurrence. *Nature Communications*, *12*(1), 6330. https://doi.org/10.1038/s41467-021-26692-z
15. Cook, B. I., Mankin, J. S., & Anchukaitis, K. J. (2018). Climate Change and Drought: From Past to Future. *Current Climate Change Reports*, *4*(2), 164–179. https://doi.org/10.1007/s40641-018-0093-2
16. Cook, B. I., Mankin, J. S., Marvel, K., Williams, A. P., Smerdon, J. E., & Anchukaitis, K. J. (2020). Twenty-First Century Drought Projections in the CMIP6 Forcing Scenarios. *Earth's Future*, *8*(6), e2019EF001461. https://doi.org/10.1029/2019EF001461
17. Coz, C. L., & Giesen, N. van de. (2020). Comparison of rainfall products over sub-saharan africa. https://doi.org/10.1175/JHM-D-18-0256.1
18. Dai, A. (2013). Increasing drought under global warming in observations and models. *Nature Climate Change*, *3*(1), 52–58. https://doi.org/10.1038/nclimate1633
19. Douville, H., Raghavan, K., Renwick, J., Allan, R. P., Arias, P. A., Barlow, M., et al. (2021). Water cycle changes. *Climate Change 2021: The Physical Science Basis. Contribution of Working Group I to 45 the*

Sixth Assessment Report of the Intergovernmental Panel on Climate Change, 1055–1210.

20. Fan, Y., & McColl, K. A. (2024). Widespread outdoor exposure to uncompensable heat stress with warming. *Communications Earth & Environment*, *5*(1), 762. https://doi.org/10.1038/s43247-024-01930-6
21. Fu, Q., & Feng, S. (2014). Responses of terrestrial aridity to global warming. *Journal of Geophysical Research: Atmospheres*, *119*(13), 7863–7875. https://doi.org/10.1002/2014JD021608
22. Funk, C., Peterson, P., Landsfeld, M., Pedreros, D., Verdin, J., Shukla, S., et al. (2015). The climate hazards infrared precipitation with stations—a new environmental record for monitoring extremes. *Scientific Data*, *2*(1), 150066. https://doi.org/10.1038/sdata.2015.66
23. Gebrechorkos, S. H., Leyland, J., Dadson, S. J., Cohen, S., Slater, L., Wortmann, M., et al. (2024). Global-scale evaluation of precipitation datasets for hydrological modelling. *Hydrology and Earth System Sciences*, *28*(14), 3099–3118. https://doi.org/10.5194/hess-28-3099-2024
24. Gebrechorkos, S. H., Sheffield, J., Vicente-Serrano, S. M., Funk, C., Miralles, D. G., Peng, J., et al. (2025). Warming accelerates global drought severity. *Nature*. https://doi.org/10.1038/s41586-025-09047-2
25. Gehne, M., Hamill, T. M., Kiladis, G. N., & Trenberth, K. E. (2016). Comparison of global precipitation estimates across a range of temporal and spatial scales. *Journal of Climate*, *29*(21), 7773–7795. https://doi.org/10.1175/JCLI-D-15-0618.1
26. Gelaro, R., McCarty, W., Suárez, M. J., Todling, R., Molod, A., Takacs, L., et al. (2017). The Modern-Era Retrospective Analysis for Research and Applications, Version 2 (MERRA-2). *Journal of Climate*, *30*(14), 5419–5454. https://doi.org/10.1175/JCLI-D-16-0758.1
27. Greve, P., Orlowsky, B., Mueller, B., Sheffield, J., Reichstein, M., & Seneviratne, S. I. (2014). Global assessment of trends in wetting and drying over land. *Nature Geoscience*, *7*(10), 716–721. https://doi.org/10.1038/ngeo2247
28. Greve, P., Roderick, M. L., Ukkola, A. M., & Wada, Y. (2019). The aridity index under global warming. *Environmental Research Letters*, *14*(12), 124006. https://doi.org/10.1088/1748-9326/ab5046
29. Gu, L., Yin, J., Slater, L. J., Chen, J., Do, H. X., Wang, H.-M., et al. (2023). Intensification of global hydrological droughts under anthropogenic climate warming. *Water Resources Research*, *59*(1), e2022WR032997. https://doi.org/10.1029/2022WR032997
30. Han, J., & Singh, V. P. (2023). A review of widely used drought indices and the challenges of drought assessment under climate change. *Environmental Monitoring and Assessment*, *195*(12), 1438. https://doi.org/10.1007/s10661-023-12062-3
31. Harris, I., Osborn, T. J., Jones, P., & Lister, D. (2020). Version 4 of the CRU TS monthly high-resolution gridded multivariate climate dataset. *Scientific Data*, *7*(1), 109. https://doi.org/10.1038/s41597-020-0453-3
32. Hawkins, E., & Sutton, R. (2009). The Potential to Narrow Uncertainty in Regional Climate Predictions. *Bulletin of the American Meteorological Society*, *90*(8), 1095–1108. https://doi.org/10.1175/2009BAMS2607.1

33. Held, I. M., & Soden, B. J. (2006). Robust Responses of the Hydrological Cycle to Global Warming. *Journal of Climate*, *19*(21), 5686–5699. https://doi.org/10.1175/JCLI3990.1
34. Hoffmann, D., Gallant, A. J. E., & Arblaster, J. M. (2020). Uncertainties in drought from index and data selection. *Journal of Geophysical Research: Atmospheres*, *125*(18), e2019JD031946. https://doi.org/10.1029/2019JD031946
35. Huang, K., Zhang, H., Cui, G., Wang, Y., Yin, M., & Du, J. (2026). Drought propagation in China: Uncertainties originate more from dataset choice than drought index selection. *Atmospheric Research*, *330*, 108555. https://doi.org/10.1016/j.atmosres.2025.108555
36. Kenawy, A. E., Al-Awadhi, T., Abdullah, M., Ostermann, F. O., & Abulibdeh, A. (2025). A multidecadal assessment of drought intensification in the middle east and north africa: The role of global warming and rainfall deficit. *Earth Systems and Environment*. https://doi.org/10.1007/s41748-025-00576-4
37. Kidd, C., Becker, A., Huffman, G. J., Muller, C. L., Joe, P., Skofronick-Jackson, G., & Kirschbaum, D. B. (2017). So, how much of the Earth's surface is covered by rain gauges? *Bulletin of the American Meteorological Society*, *98*(1), 69–78. https://doi.org/10.1175/BAMS-D-14-00283.1
38. Kim, Y., Garcia, M., & Johnson, M. S. (2023). Land-atmosphere coupling constrains increases to potential evaporation in a warming climate: Implications at local and global scales. *Earth's Future*, *11*(2), e2022EF002886. https://doi.org/10.1029/2022EF002886
39. Kosaka, Y., Kobayashi, S., Harada, Y., Kobayashi, C., Naoe, H., Yoshimoto, K., et al. (2024). The JRA-3Q Reanalysis. *Journal of the Meteorological Society of Japan. Ser. II*, *102*(1), 49–109. https://doi.org/10.2151/jmsj.2024-004
40. Liu, H., Wang, X., Liang, C., Xue, P., Wang, Z., Chen, Y., & Zhang, M. (2024). Divergent nonlinear trends of global drought and its multivariate characteristics. *Journal of Hydrology*, *630*, 130759. https://doi.org/10.1016/j.jhydrol.2024.130759
41. Liu, X., Zhu, X., Pan, Y., Li, S., Liu, Y., & Ma, Y. (2016). Agricultural drought monitoring: Progress, challenges, and prospects. *Journal of Geographical Sciences*, *26*(6), 750–767. https://doi.org/10.1007/s11442-016-1297-9
42. Mankin, J. S., Seager, R., Smerdon, J. E., Cook, B. I., & Williams, A. P. (2019). Mid-latitude freshwater availability reduced by projected vegetation responses to climate change. *Nature Geoscience*, *12*(12), 983–988. https://doi.org/10.1038/s41561-019-0480-x
43. Mankin, K. R., Mehan, S., Green, T. R., & Barnard, D. M. (2025). Review of gridded climate products and their use in hydrological analyses reveals overlaps, gaps, and the need for a more objective approach to selecting model forcing datasets. *Hydrology and Earth System Sciences*, *29*(1), 85–108. https://doi.org/10.5194/hess-29-85-2025
44. McColl, K. A., Roderick, M. L., Berg, A., & Scheff, J. (2022). The terrestrial water cycle in a warming world. *Nature Climate Change*, *12*(7), 604–606. https://doi.org/10.1038/s41558-022-01412-7
45. Milly, P. C. D., & Dunne, K. A. (2016). Potential evapotranspiration and continental drying. *Nature Climate Change*, *6*(10), 946–949. https://doi.org/10.1038/nclimate3046

46. Mishra, A. K., & Singh, V. P. (2010). A review of drought concepts. *Journal of Hydrology*, *391*(1–2), 202–216. https://doi.org/10.1016/j.jhydrol.2010.07.012
47. Mukherjee, S., Mishra, A., & Trenberth, K. E. (2018). Climate change and drought: A perspective on drought indices. *Current Climate Change Reports*, *4*(2), 145–163. https://doi.org/10.1007/s40641-018-0098-x
48. Muñoz-Sabater, J., Dutra, E., Agustí-Panareda, A., Albergel, C., Arduini, G., Balsamo, G., et al. (2021). ERA5-land: A state-of-the-art global reanalysis dataset for land applications. *Earth System Science Data*, *13*(9), 4349–4383. https://doi.org/10.5194/essd-13-4349-2021
49. Mwinjuma, M., Wang, R., Mtupili, M., & Twaha, M. (2026). Comparisons of SPI and SPEI in capturing drought dynamics: A global assessment across arid and humid regions. *Atmospheric Research*, *329*, 108475. https://doi.org/10.1016/j.atmosres.2025.108475
50. Niu, Q., She, D., Xia, J., Zhang, Q., Zhang, Y., & Wang, T. (2025). Uncertainty analysis of global meteorological drought in CMIP6 projections. *Climatic Change*, *178*(4), 75–98. https://doi.org/10.1007/s10584-025-03919-2
51. Obarein, O. A., & Lee, C. C. (2025). ERA5 reproduces key features of global precipitation trends in a warming climate. *International Journal of Climatology*, *45*(9), e8877. https://doi.org/10.1002/joc.8877
52. OECD. (2025). *Towards a drier world: Global drought outlook*. Retrieved from https://www.oecd.org/en/publications/global-drought-outlook_d492583a-en/full-report/towards-a-drier-world_6f10e2e5.html
53. Ogunrinde, A. T., Adigun, P., Xue, X., Dairaku, K., Shah, S. A., & Adawa, I. S. (2026). Probabilistic quantification of global drought risk amplification from temperature-enhanced evapotranspiration under climate change. *Geoscience Frontiers*, *17*(2), 102235. https://doi.org/10.1016/j.gsf.2025.102235
54. Otkin, J. A., Svoboda, M., Hunt, E. D., Ford, T. W., Anderson, M. C., Hain, C., & Basara, J. B. (2018). Flash droughts: a review and assessment of the challenges imposed by rapid-onset droughts in the United States. *Bulletin of the American Meteorological Society*, *99*(5), 911–919.
55. Penman, H. L. (1948). Natural evaporation from open water, hare soil and grass. *Proceedings of the Royal Society of London. Series A Mathematical and Physical Sciences*, *193*(1032), 120–145. https://doi.org/10.1098/rspa.1948.0037
56. Rajulapati, C. R., Papalexiou, S. M., Clark, M. P., Razavi, S., Tang, G., & Pomeroy, J. W. (2020). Assessment of extremes in global precipitation products: How reliable are they? *Journal of Hydrometeorology*, *21*(12), 2855–2873. https://doi.org/10.1175/JHM-D-20-0040.1
57. Roderick, M. L., Rotstayn, L. D., Farquhar, G. D., & Hobbins, M. T. (2007). On the attribution of changing pan evaporation. *Geophysical Research Letters*, *34*(17). https://doi.org/10.1029/2007GL031166
58. Roderick, M. L., Greve, P., & Farquhar, G. D. (2015). On the assessment of aridity with changes in atmospheric CO2. *Water Resources Research*, *51*(7), 5450–5463.

https://doi.org/10.1002/2015WR017031

59. Scheff, J., & Frierson, D. M. W. (2014). Scaling potential evapotranspiration with greenhouse warming. *Journal of Climate*, *27*(4), 1539–1558. https://doi.org/10.1175/JCLI-D-13-00233.1
60. Schneider, U., Fuchs, T., Meyer-Christoffer, A., & Rudolf, B. (2008). Global precipitation analysis products of the GPCC. *Global Precipitation Climatology Centre (GPCC), DWD, Internet Publikation*, *112*, 3819–3837.
61. Seager, R., Naik, N., & Vecchi, G. A. (2010). Thermodynamic and Dynamic Mechanisms for Large-Scale Changes in the Hydrological Cycle in Response to Global Warming*. *Journal of Climate*, *23*(17), 4651–4668. https://doi.org/10.1175/2010JCLI3655.1
62. Seneviratne, S. I., Corti, T., Davin, E. L., Hirschi, M., Jaeger, E. B., Lehner, I., et al. (2010). Investigating soil moisture–climate interactions in a changing climate: A review. *Earth-Science Reviews*, *99*(3–4), 125–161. https://doi.org/10.1016/j.earscirev.2010.02.004
63. Sheffield, J., Wood, E. F., & Roderick, M. L. (2012). Little change in global drought over the past 60 years. *Nature*, *491*(7424), 435–438. https://doi.org/10.1038/nature11575
64. Shi, L., Feng, P., Wang, B., Liu, D. L., & Yu, Q. (2020). Quantifying future drought change and associated uncertainty in southeastern australia with multiple potential evapotranspiration models. *Journal of Hydrology*, *590*, 125394. https://doi.org/10.1016/j.jhydrol.2020.125394
65. Stahle, L., & Wold, S. (1989). Analysis of variance (ANOVA). *Chemometrics and Intelligent Laboratory Systems*, *6*(4), 259–272. https://doi.org/10.1016/0169-7439(89)80095-4
66. Stedinger, J., Vogel, R., Foufoula-Georgiou, E., & Maidment, D. R. (1993). Handbook of hydrology. *McGraw-Hill, Inc.*, *New York, USA*.
67. Su, J., Miao, C., Zwiers, F., Beck, H., Jones, P., Sun, Q., et al. (2026). Precipitation observing network gaps limit climate change impact assessment. *Nature*, *652*(8108), 119–125. https://doi.org/10.1038/s41586-026-10300-5
68. Sun, J., Zhang, Q., Xu, Y. J., Liu, X., Chen, L., Zhang, G., & Wu, Y. (2025). Will drought evolution accelerate under future climate? *Journal of Hydrology*, *650*, 132552. https://doi.org/10.1016/j.jhydrol.2024.132552
69. Sun, Q., Miao, C., Duan, Q., Ashouri, H., Sorooshian, S., & Hsu, K.-L. (2018). A review of global precipitation data sets: Data sources, estimation, and intercomparisons. *Reviews of Geophysics*, *56*(1), 79–107. https://doi.org/10.1002/2017RG000574
70. Swann, A. L. S., Hoffman, F. M., Koven, C. D., & Randerson, J. T. (2016). Plant responses to increasing CO2 reduce estimates of climate impacts on drought severity. *Proceedings of the National Academy of Sciences*, *113*(36), 10019–10024. https://doi.org/10.1073/pnas.1604581113
71. Tan, X., Wu, Y., Liu, B., & Chen, S. (2020). Inconsistent changes in global precipitation seasonality in seven precipitation datasets. *Climate Dynamics*, *54*(5), 3091–3108. https://doi.org/10.1007/s00382-020-05158-w
72. Tan, Y. X., Ng, J. L., & Huang, Y. F. (2023). Quantitative analysis of input data uncertainty for SPI and SPEI in peninsular malaysia based on the bootstrap method. *Hydrological Sciences Journal*, *68*(12),

1724–1737. https://doi.org/10.1080/02626667.2023.2232348

73. Tang, L. I., & McColl, K. A. (2025). Radiative–convective equilibrium over an idealized land surface with fixed soil moisture. *Journal of Climate*, *38*(22), 6639–6659. https://doi.org/10.1175/JCLI-D-24-0438.1
74. Tomas-Burguera, M., Vicente-Serrano, S. M., Peña-Angulo, D., Domínguez-Castro, F., Noguera, I., & El Kenawy, A. (2020). Global characterization of the varying responses of the standardized precipitation evapotranspiration index to atmospheric evaporative demand. *Journal of Geophysical Research: Atmospheres*, *125*(17), e2020JD033017. https://doi.org/10.1029/2020JD033017
75. Trenberth, K. E., Dai, A., van der Schrier, G., Jones, P. D., Barichivich, J., Briffa, K. R., & Sheffield, J. (2014). Global warming and changes in drought. *Nature Climate Change*, *4*(1), 17–22. https://doi.org/10.1038/nclimate2067
76. Ukkola, A. M., De Kauwe, M. G., Roderick, M. L., Abramowitz, G., & Pitman, A. J. (2020). Robust future changes in meteorological drought in CMIP6 projections despite uncertainty in precipitation. *Geophysical Research Letters*, *47*(11), e2020GL087820. https://doi.org/10.1029/2020GL087820
77. Vicente-Serrano, S. M., Beguería, S., & López-Moreno, J. I. (2010). A Multiscalar Drought Index Sensitive to Global Warming: The Standardized Precipitation Evapotranspiration Index. *Journal of Climate*, *23*(7), 1696–1718. https://doi.org/10.1175/2009JCLI2909.1
78. Vicente-Serrano, S. M., Peña-Angulo, D., Beguería, S., Domínguez-Castro, F., Tomás-Burguera, M., Noguera, I., et al. (2022). Global drought trends and future projections. *Philosophical Transactions of the Royal Society A: Mathematical, Physical and Engineering Sciences*, *380*(2238), 20210285. https://doi.org/10.1098/rsta.2021.0285
79. Wang, F., Wang, Z., Yang, H., & Zhao, Y. (2018). Study of the temporal and spatial patterns of drought in the yellow river basin based on SPEI. *Science China Earth Sciences*, *61*(8), 1098–1111. https://doi.org/10.1007/s11430-017-9198-2
80. Wang, K., Mou, W., Cai, H., Yin, C., Li, Y., Allan, R. P., et al. (2026). ERA5 overestimates land drying trend from 1980 to 2023 by more than 100%. *Science Bulletin*. https://doi.org/10.1016/j.scib.2026.01.045
81. Wang, Q., Zeng, J., Qi, J., Zhang, X., Zeng, Y., Shui, W., et al. (2021a). A multi-scale daily SPEI dataset for drought characterization at observation stations over mainland China from 1961 to 2018. *Earth System Science Data*, *13*(2), 331–341. https://doi.org/10.5194/essd-13-331-2021
82. Wang, T., Li, Z., Ma, Z., Gao, Z., & Tang, G. (2023). Diverging identifications of extreme precipitation events from satellite observations and reanalysis products: A global perspective based on an object-tracking method. *Remote Sensing of Environment*, *288*, 113490. https://doi.org/10.1016/j.rse.2023.113490
83. Wang, W., Li, C., Xing, W., & Fu, J. (2017). Projecting the potential evapotranspiration by coupling different formulations and input data reliabilities: The possible uncertainty source for climate change impacts on hydrological regime. *Journal of Hydrology*, *555*, 298–313. https://doi.org/10.1016/j.jhydrol.2017.10.023

84. Wang, W., Wang, J., & Romanowicz, R. (2021b). Uncertainty in SPI calculation and its impact on drought assessment in different climate regions over China. *Journal of Hydrometeorology*. https://doi.org/10.1175/JHM-D-20-0256.1

85. Wu, C., Yeh, P. J.-F., Ju, J., Chen, Y.-Y., Xu, K., Dai, H., et al. (2021). Assessing the spatiotemporal uncertainties in future meteorological droughts from CMIP5 models, emission scenarios, and bias corrections. https://doi.org/10.1175/JCLI-D-20-0411.1

86. Xiang, K., Li, Y., Horton, R., & Feng, H. (2020). Similarity and difference of potential evapotranspiration and reference crop evapotranspiration – a review. *Agricultural Water Management*, *232*, 106043. https://doi.org/10.1016/j.agwat.2020.106043

87. Xiang, Y., Chen, J., Li, L., Peng, T., & Yin, Z. (2021). Evaluation of eight global precipitation datasets in hydrological modeling. *Remote Sensing*, *13*(14), 2831. https://doi.org/10.3390/rs13142831

88. Xie, P., Chen, M., & Shi, W. (2010). CPC unified gauge-based analysis of global daily precipitation. In *Preprints, 24th Conf. on Hydrology, Atlanta, GA, Amer. Meteor. Soc* (Vol. 2). Retrieved from https://ams.confex.com/ams/90annual/techprogram/paper_163676.htm

89. Yang, Y., & Roderick, M. L. (2019). Radiation, surface temperature and evaporation over wet surfaces. *Quarterly Journal of the Royal Meteorological Society*, *145*(720), 1118–1129. https://doi.org/10.1002/qj.3481

90. Yang, Y., Roderick, M. L., Zhang, S., McVicar, T. R., & Donohue, R. J. (2019). Hydrologic implications of vegetation response to elevated CO2 in climate projections. *Nature Climate Change*, *9*(1), 44–48. https://doi.org/10.1038/s41558-018-0361-0

91. Yuan, X., Wang, Y., Ji, P., Wu, P., Sheffield, J., & Otkin, J. A. (2023). A global transition to flash droughts under climate change. *Science*, *380*(6641), 187–191. https://doi.org/10.1126/science.abn6301

92. Zhao, T., & Dai, A. (2022). CMIP6 model-projected hydroclimatic and drought changes and their causes in the twenty-first century. *Journal of Climate*, *35*(3), 897–921. https://doi.org/10.1175/JCLI-D-21-0442.1

93. Zhou, M., Haseeb, M., Tahir, Z., Mahmood, S. A., Arif, H., Abdullah-Al-Wadud, M., & Tariq, A. (2025). Multiscale drought assessment with analyzing agricultural, meteorological, and hydrological impacts multi-index approaches (1991–2021). *Theoretical and Applied Climatology*, *156*(5), 289–310. https://doi.org/10.1007/s00704-025-05494-z

94. Zhou, S., & Yu, B. (2024). Physical basis of the potential evapotranspiration and its estimation over land. *Journal of Hydrology*, *641*, 131825. https://doi.org/10.1016/j.jhydrol.2024.131825

95. Zhou, S., & Yu, B. (2025a). Neglecting land–atmosphere feedbacks overestimates climate-driven increases in evapotranspiration. *Nature Climate Change*, 1–8. https://doi.org/10.1038/s41558-025-02428-5

96. Zhou, S., & Yu, B. (2025b). Reconciling the discrepancy in projected global dryland expansion in a warming world. *Global Change Biology*, *31*(3), e70102. https://doi.org/10.1111/gcb.70102

97. Zhou, S., Williams, A. P., Lintner, B. R., Findell, K. L., Keenan, T. F., Zhang, Y., & Gentine, P. (2022). Diminishing seasonality of subtropical water availability in a warmer world dominated by soil moisture–atmosphere feedbacks. *Nature Communications*, *13*(1), 5756. https://doi.org/10.1038/s41467-022-33473-9

Figures

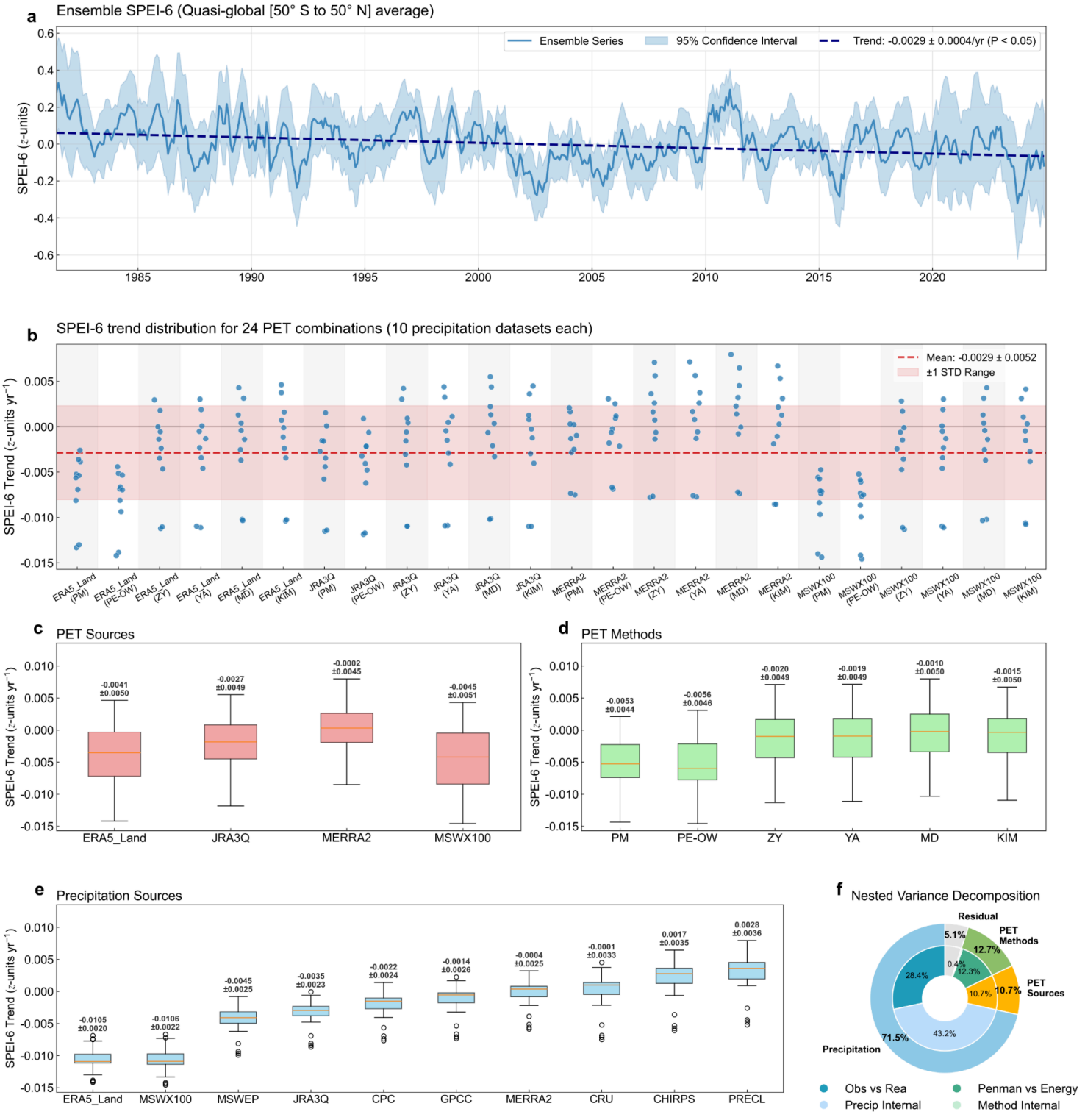


Figure 1

Quasi-global (50° S to 50° N) average 6-month SPEI trend (*z*-units yr^{-1}) and associated uncertainty analysis. (**a**). Combined SPEI time series and trend of all precipitation sources (240 datasets). (**b**) SPEI trends derived from 240 datasets. (**c–e**) Box-line plots illustrating SPEI trend uncertainties arising from PET methods (**c**), PET data sources (**d**), and precipitation sources (**e**). (**f**) Relative contributions of different sources to SPEI trend uncertainty. The time series for trend extraction were averaged over the quasi-global land areas (50°S–50°N) as CHIRPS is available at 50°S to 50° N, excluding regions with an average annual rainfall below 180 mm (Supplementary Fig. 7). This rainfall threshold was derived from the mean of ten precipitation sources. The shaded envelope in (**a**) denotes the 95% confidence interval calculated from different datasets, reflecting uncertainty arising from datasets differences. The x-axis in panel (**b**) denotes the SPEI variants, with labels specifying the PET data source (ERA5_Land, JRA3Q, MERRA2, and MSWX100) and algorithm (PE-OW, PM, ZY, YA, MD, and KIM). The “obs” in panel (f) include precipitation sources from CRU, GPCC, CPC, PRECL, CHIRPS, and MSWEP, the rest four sources are classified as “Rea”. Penman-based PET methods contain PE-OW and PM whereas energy-based PET methods include ZY, YA, MD and KIM.

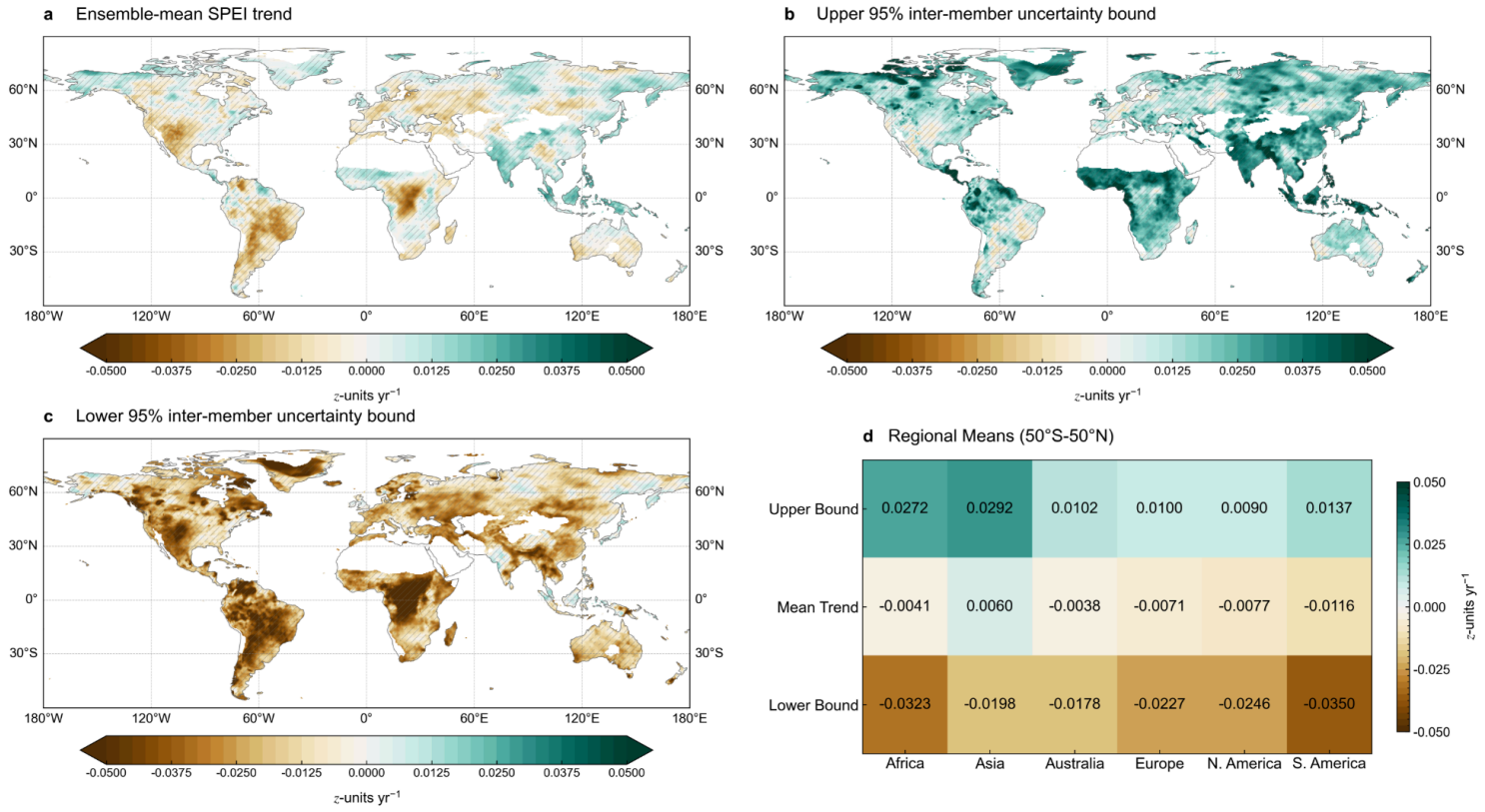
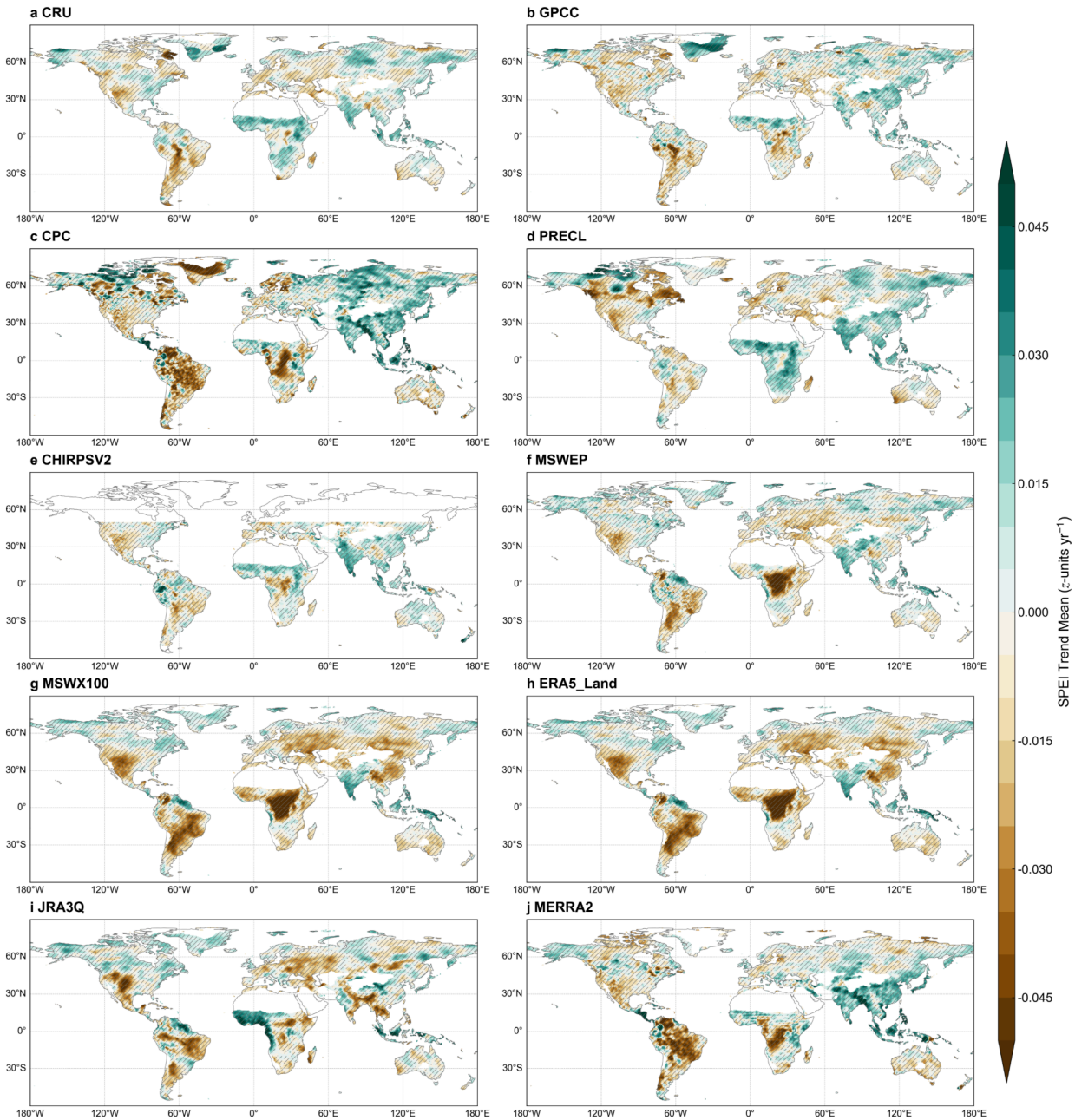


Figure 2

Spatial patterns and regional means of the 6-month SPEI trend (z-units yr^{-1}) for 1981–2024. (**a**) Ensemble-mean SPEI trend derived from 240 SPEI series. (**b**) Upper inter-member uncertainty bound of the SPEI trend, defined as the 95th percentile of the 240 member-specific trends. (**c**) Lower inter-member uncertainty bound of the SPEI trend, defined as the 5th percentile of the 240 member-specific trends.

Stippling indicates grid cells where the ensemble-mean trend is statistically significant ($P < 0.05$). (**d**) Regional means of the three fields shown in (**a**)–(**c**). Regional mean trends were extracted over the quasi-global land areas (50°S–50°N), excluding regions with an average annual rainfall below 180 mm. The regional boundaries used for calculating regional means are shown in Supplementary Fig. 7.

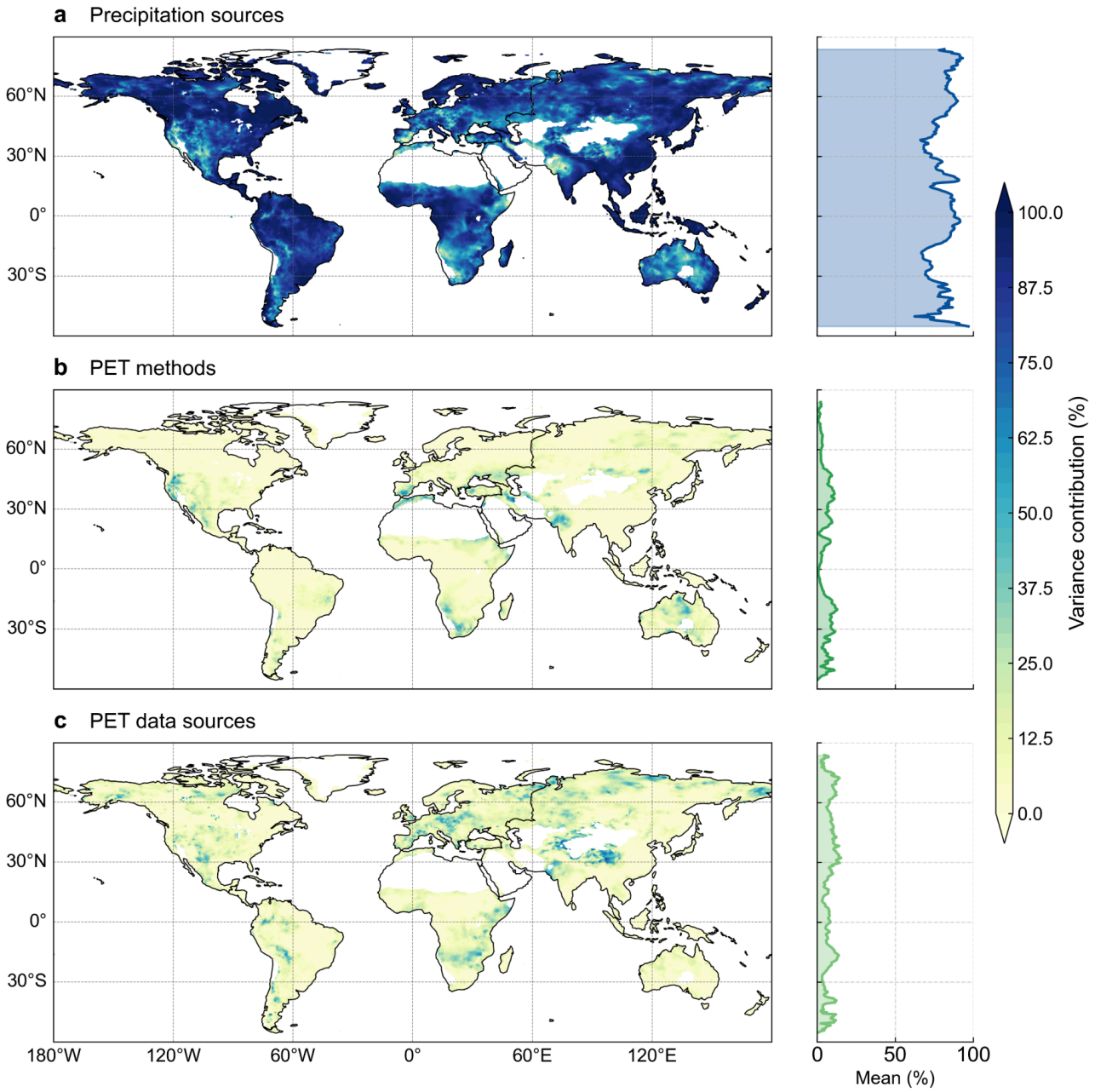


k Regional Means (50°S-50°N)

	CRU	GPCC	CPC	PRECL	CHIRPSV2	MSWEP	MSWX100	ERA5_Land	JRA3Q	MERRA2
Quasi-Global	-0.0000	-0.0014	-0.0028	0.0028	0.0016	-0.0046	-0.0111	-0.0110	-0.0036	-0.0009
Africa	0.0082	-0.0012	-0.0079	0.0137	0.0022	-0.0125	-0.0203	-0.0207	0.0022	-0.0042
Asia	0.0032	0.0062	0.0179	0.0106	0.0082	0.0038	-0.0040	-0.0036	-0.0025	0.0199
Australia	-0.0018	-0.0001	-0.0079	-0.0047	0.0029	-0.0023	-0.0070	-0.0068	-0.0024	-0.0075
Europe	-0.0077	-0.0064	-0.0024	-0.0093	-0.0036	-0.0104	-0.0118	-0.0106	-0.0084	-0.0000
N. America	-0.0026	-0.0063	-0.0091	-0.0095	-0.0047	-0.0050	-0.0113	-0.0110	-0.0095	-0.0079
S. America	-0.0093	-0.0085	-0.0201	-0.0047	-0.0029	-0.0082	-0.0167	-0.0166	-0.0093	-0.0196

Figure 3

Spatial patterns and regional means of the 6-month SPEI trend (z-units yr^{-1}) for 1981–2024, based on the ensemble mean of precipitation sources per grid cell. (**a-j**) Average SPEI trend for each of the 10 precipitation datasets, derived by averaging the corresponding members from the total 240 SPEI series classified by precipitation source. The 10 precipitation sources are: CRU (**a**), GPCC (**b**), CPC (**c**), PRECL (**d**), CHIRPS-V2 (**e**), MSWEP (**f**), MSWX100 (**g**), ERA5_Land (**h**), JRA3Q (**i**), and MERRA2 (**j**). (**k**) shows regional means extracted from precipitation product-specific SPEI trends shown in (**a-j**). Stippling indicates statistical significance ($P < 0.05$) where applicable. Regional averaging is performed over the quasi-global land areas (50°S–50°N), excluding regions with average annual rainfall below 180 mm. The regional boundaries used for calculating regional means can be found in Supplementary Fig. 7.



d Regional Means (50°S-50°N) (%)

Quasi-Global	Africa	Asia	Australia	Europe	N. America	S. America	
78.1	74.2	78.9	68.0	68.1	77.6	85.9	Precipitation sources
6.5	7.4	5.5	11.3	12.0	7.7	3.5	PET methods
8.4	9.8	9.4	4.6	14.8	8.6	6.3	PET data sources

Figure 4

Spatial distribution and regional statistics of uncertainty sources in the 6-month SPEI trends (1981–2024). (**a-c**) Fraction of variance explained by (**a**) precipitation sources, (**b**) potential evapotranspiration (PET) methods, and (**c**) PET data sources, based on ANOVA. (**d**) Regional mean variance contributions extracted from the spatial fields in (**a-c**). Regional averaging is performed over the quasi-global land areas (50°S–50°N), excluding regions with average annual rainfall below 180 mm. The regional

boundaries used for calculating regional means correspond to those in Supplementary Fig. 7. The spatial distribution of residuals in the ANOVA analysis is not shown.

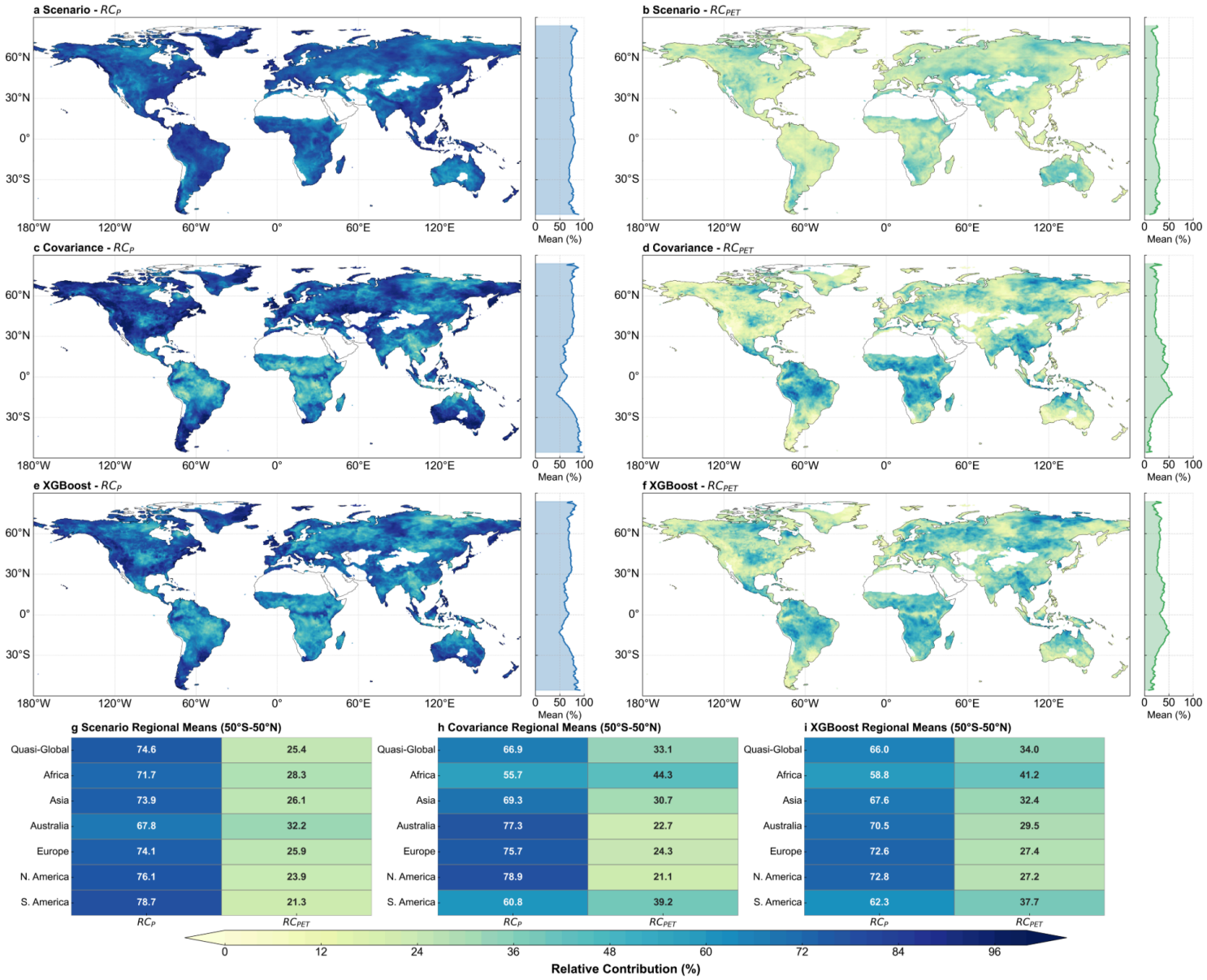


Figure 5

Spatial distribution and regional statistics of the contributions of precipitation (RC_P) and potential evapotranspiration (RC_{PET}) to SPEI trends based on historical data. (**a, c, e**) Spatial patterns of RC_P calculated using the Scenario, Covariance, and XGBoost methods, respectively. (**b, d, f**) Spatial patterns of RC_{PET} derived from the corresponding three methods. (**g-i**) Regional mean RC_P and RC_{PET} extracted from the spatial fields for the Scenario, Covariance, and XGBoost methods, respectively. Regional averaging is performed over the quasi-global land areas (50°S–50°N), excluding regions with average annual rainfall below 180 mm. The regional boundaries correspond to those detailed in Supplementary Fig. 7.

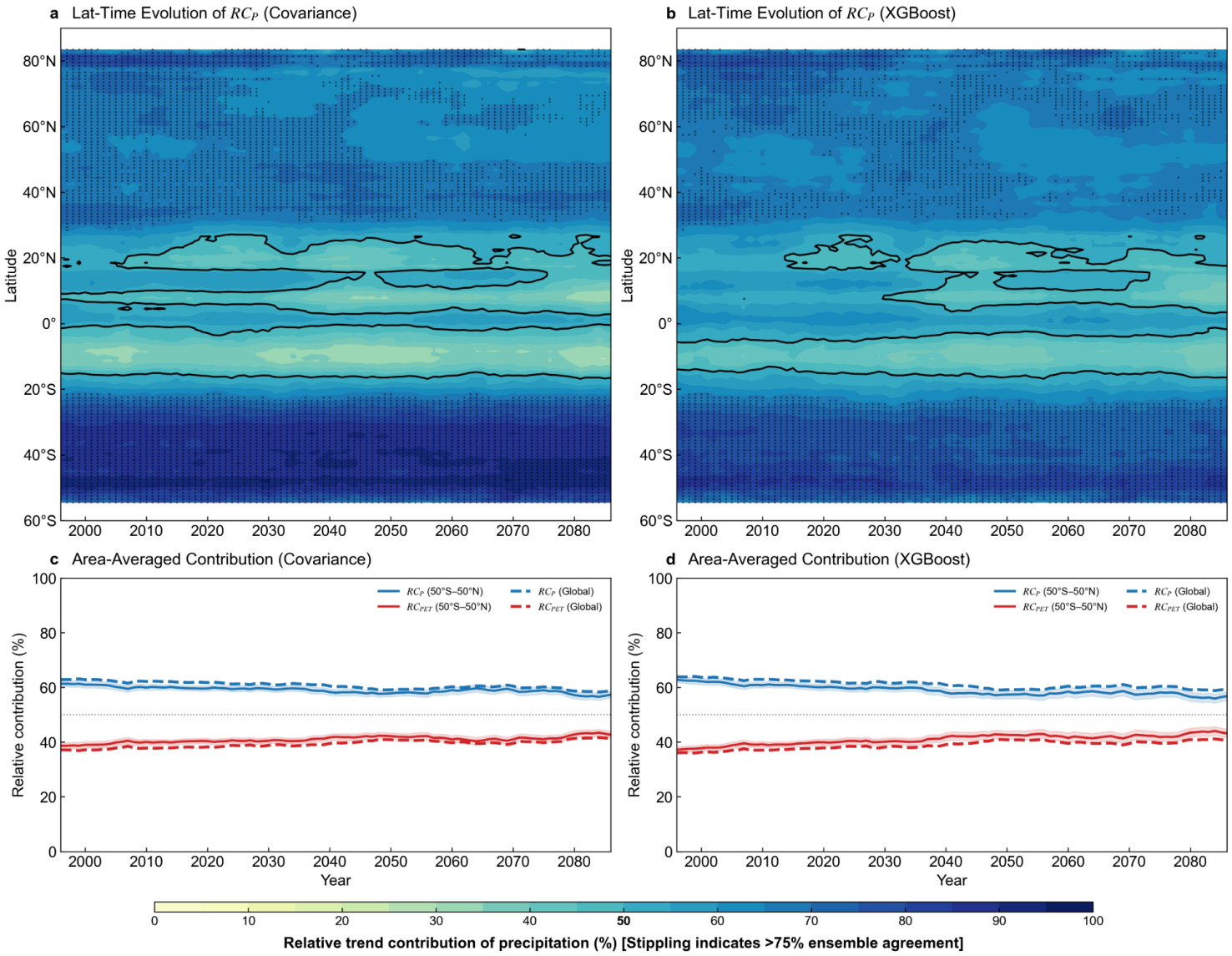


Figure 6

Temporal evolution of the latitude-averaged and regional mean contributions of precipitation (RC_P) and potential evapotranspiration (RC_{PET}) to SPEI trends under future climate change. (**a, b**) Latitude-time evolution of the RC_P calculated using the (**a**) Covariance and (**b**) XGBoost methods. (**c, d**) Time series of the regional mean contributions of RC_P (blue lines) and RC_{PET} (red lines) derived from the (**c**) Covariance and (**d**) XGBoost methods. In (**c**) and (**d**), solid lines represent the quasi-global average over the quasi-global land areas (50°S–50°N), while lines represent the global land average. Regional and latitudinal averaging excludes regions with average annual rainfall below 180 mm.

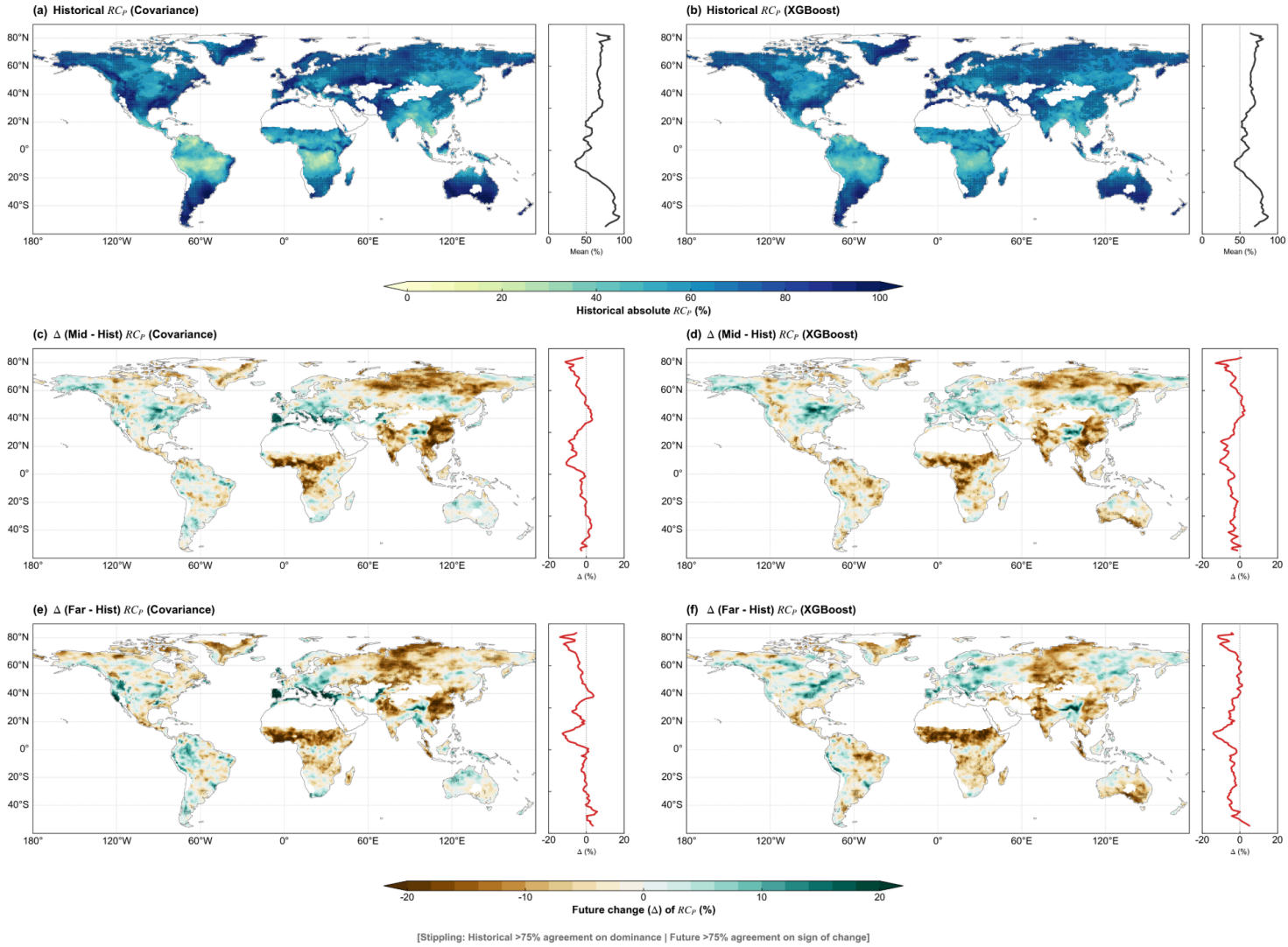


Figure 7

Spatial distribution and future changes of precipitation contributions (RC_P) to SPEI trends derived from the Covariance and XGBoost methods. (**a, b**) Historical (1996–2015) mean RC_P calculated using the Covariance (**a**) and XGBoost (**b**) methods. (**c, d**) Projected mid-future (2036–2055) changes (Δ) in RC_P relative to the historical baseline for the (**c**) Covariance and (**d**) XGBoost methods. (**e, f**) Projected far-future (2066–2085) changes (Δ) in RC_P relative to the historical baseline for the (**e**) Covariance and (**f**) XGBoost methods. Stippling indicates areas with robust multi-model consensus (e.g., >75% agreement on the dominant driver for historical means, and >75% agreement on the sign of change for future projections).

Supplementary Files

This is a list of supplementary files associated with this preprint. Click to download.

- CEESuppInfoxiao.pdf